MNRAS 000, 1–20 (2020) Preprint 6 March 2020 Compiled using MNRAS LATEX style file v3.0

The halo model as a versatile tool to predict intrinsic alignments

Maria Cristina Fortuna[1]★, Henk Hoekstra[1], Benjamin Joachimi[2], Harry Johnston[2], Nora Elisa Chisari[3], Christos Georgiou[1], Constance Mahony[2]
[1]Leiden Observatory, Leiden University, PO Box 9513, Leiden, NL-2300 RA, The Netherlands
[2]Department of Physics and Astronomy, University College London, Gower Street, London WC1E 6BT, UK
[3]Institute for Theoretical Physics, Utrecht University, Princetonplein 5, 3584 CE Utrecht, The Netherlands

Accepted XXX. Received YYY; in original form ZZZ

ABSTRACT

Intrinsic alignments (IAs) of galaxies are an important contaminant for cosmic shear studies, but the modelling is complicated by the dependence of the signal on the source galaxy sample. In this paper, we use the halo model formalism to capture this diversity and examine its implications for a Stage III cosmic shear survey. We account for the different IA signatures at large and small scales as well for the different contribution from central/satellite and red/blue galaxies. We inform our model using the most recent observational findings: we include a luminosity dependence at both large and small scales and a radial dependence of the signal within the halo. We predict the impact of the total IA signal on the lensing angular power spectra, including the current uncertainties from the IA best-fits to illustrate the range of possible impact on the lensing signal: the lack of constraints for fainter galaxies is the main source of uncertainty for our predictions of the IA signal. We investigate how well the widely used non-linear alignment model can capture the complexity of the IA signal and find that while for Stage III surveys it is flexible enough, in the case of a Stage IV survey, this can lead to 1σ bias on Ω_m.

Key words: cosmology: theory – gravitational lensing: weak – galaxies: haloes – galaxies: statistics

1 INTRODUCTION

As the light of distant galaxies travels towards us, it is deflected by matter inhomogeneities. The cumulative effect of these small distortions leads to a preferential apparent alignment of galaxy shapes, a phenomenon called weak lensing. The resulting correlation of galaxy shapes (*cosmic shear*) provides direct information on the matter distribution in the Universe as well as the effect of dark energy on the geometry and the growth of structures (e.g Bartelmann & Schneider 2001; Kilbinger 2015). However, extracting cosmological parameter estimates from weak lensing surveys is challenging due to a number of systematic errors it is prone to. On the measurements side, the main sources of bias come from the uncertainty in the source redshift distributions and the actual shape measurements, for which great improvements have been achieved in the last decades, due to advances in both image simulations and shape measurement algorithms (Kannawadi et al. 2019; Mandelbaum 2018, for a dedicated review).

On the modelling side, a naive interpretation of cosmic shear would relate the observed correlations between galaxy orientations as solely arising from the lensing effect of matter. In reality, galaxies form and live inside dark matter haloes and they are continuously exposed to the gravitational interaction with the surrounding matter distribution. This leads to the coherent alignment induced by the underlying tidal field on physically near galaxies, the so-named intrinsic alignment (IA) (Joachimi et al. 2015; Kiessling et al. 2015; Kirk et al. 2015; Troxel & Ishak 2015, for extensive reviews). If not properly accounted, IA can affect the inferred properties of the matter distribution from lensing. In the perspective of high precision surveys such as Euclid[1] (Laureijs et al. 2011) and LSST[2] (Abell et al. 2009), which aim to measure cosmological parameters with an accuracy better

★ E-mail: fortuna@strw.leidenuniv.nl (Leiden Observatory)

[1] https://www.euclid-ec.org
[2] https://www.lsst.org

than a percent, it is crucial to properly model the impact of IA and to quantify the level of precision required in our models and IA constraints (Joachimi & Bridle 2010; Kirk et al. 2010; Krause et al. 2016).

One of the challenges in mitigating the effect of IA comes from the differences between the samples employed in studies of IA and in cosmic shear. Pressure supported (red/elliptical) galaxies are more subjected to the effect of tidal fields and tend to stretch their shapes in the direction of the matter overdensities (Catelan et al. 2001). This turns into a non-negligible IA signal, observationally constrained by a number of works (e.g. Mandelbaum et al. 2006; Hirata et al. 2007; Joachimi et al. 2011; Singh et al. 2015; Johnston et al. 2019, hereafter J19). On the other hand, disc, rotationally supported (blue) galaxies preferentially align their spins through a torque mechanism. Although this has been observed in simulations, there is no consensus on the final predictions due to the different implementations of hydrodynamics and baryonic feedback (e.g. Chisari et al. 2015b; Tenneti et al. 2016; Codis et al. 2018; Kraljic et al. 2019). From an observational point of view, the alignment of blue galaxies has not been detected yet, neither at low and intermediate redshifts (Mandelbaum et al. 2011; Samuroff et al. 2018, J19), nor at high redshifts (Tonegawa et al. 2018).

For this reason, to maximise the signal-to-noise ratio, the majority of IA analyses focus on low redshift red galaxies, while cosmic shear surveys typically span a much broader range in redshift and do not make any colour selection. A proper re-scaling of IA predictions, weighted by the fraction of red galaxies in the sample, is then required in order to correctly account for the alignment contribution to the signal.

While the aforementioned alignment mechanisms describe the behaviour of the central galaxies well, the picture at small scales is complicated by the intra-halo tidal fields, galaxy mergers and halo assembly history, as well as AGN feedback and winds (Soussana et al. 2020; Tenneti et al. 2017). Pereira et al. (2008) and Pereira & Bryan (2010) investigated the satellite halo alignment in simulations, finding an overall tendency of satellites to point radially towards the centre of the host halo, due to a continuous torquing mechanism that aligns their major axes in the direction of the gravitational potential gradient during their orbits. Motivated by their findings, a halo model description of this alignment term was developed by Schneider & Bridle (2010, hereafter SB10). However, Sifón et al. (2015) did not find observational evidence for satellite alignment in clusters. Similarly, Chisari et al. (2014) explored the alignment signal around stacked clusters and found it to be consistent with zero. Huang et al. (2018) pointed out that the signal depends on the shape algorithm used, a feature further confirmed by Georgiou et al. (2019a, hereafter G19).

Recently, J19 and G19 investigated the alignment signal in the overlapping region between the Kilo Degree Survey[3] (KiDS, de Jong et al. 2013; Kuijken et al. 2019) and the Galaxy and Mass Assembly survey (GAMA, Driver et al. 2011). The detected IA signal provides evidence that a simple dichotomy between red and blue galaxies is not sufficient to capture the entire physics of the IA signal. In particular, G19 observed a scale dependence of the satellite alignment with satellite shapes radially aligned at small radii and a vanishing signal towards larger scales. As a consequence, the tendency of satellites to be randomly orientated at large scales suppresses the the overall IA signal, as observed by J19. Therefore, even in the linear regime, where the IA signal can be modelled through the linear alignment model (LA, Hirata & Seljak 2004), the evolution of the satellite fraction in the sample can imprint a varying amplitude to the signal, a feature never explored by any forecasting analysis so far.

Cosmic shear analyses employ tomographic binning to investigate the growth of structures and better constrain cosmological parameters. Since these surveys are flux-limited, the tomography imprints an indirect galaxy selection, including only the most luminous galaxies in the high redshift bins. As satellites are intrinsically fainter, this turns into a satellite cut at high redshifts. Satellites contribute predominantly a random signal at large scales and therefore can induce a modulation of the IA signal over the bins, suppressing it at large scales and boosting it at small scales, at low redshifts. The extrapolation of the results from IA studies then requires some care, since the majority of them limit their analyses to low-to-intermediate redshifts.

In addition, a luminosity dependence of the IA signal is currently under debate. While it has been observed for large luminous galaxies (Mandelbaum et al. 2006; Hirata et al. 2007; Joachimi et al. 2011; Singh et al. 2015), J19 has found no evidence for any luminosity scaling, hinting towards a more complex sample dependence. Similarly, two studies suggest a different behaviour for the satellite alignment signal, with Huang et al. (2018) detecting a more prominent alignment for the brightest satellites located close to the central galaxy, while G19 do not observe any luminosity trend in galaxy groups, but confirm a radial dependent signal. As for the large scales, a luminosity dependence of the satellite alignment can significantly change the contamination for a lensing survey, where the low redshift tomographic bins are dominated by faint satellites.

Understanding the sample dependence in the IA mechanism is a key feature to properly model it in the broader case of a cosmic shear galaxy sample. In this paper we investigate the impact of satellite galaxy alignment both at large and small scales. We provide a unified framework to incorporate all of the sample dependencies that emerged from observations, through the halo model formalism. We also explore the areas of tension between different measurements in the literature, trying to incorporate all of the available information as well as the current uncertainties in our predictions. We base our model on SB10, including the scale dependent signal measured in G19 and the luminosity dependence suggested by Huang et al. (2018).

The paper is organised as following. In Sec. 2 we describe the mock data we use to simulate a cosmic shear survey, for which we employ the Marenostrum Institut de Ciències de l'Espai Simulations (MICE). We build our mock to resemble a Stage III survey, mainly inspired by the final data release of KiDS. Sec. 3 introduces our model at large scales. We explore the possibility that part of the tension around the luminosity scaling of the IA signal is caused by neglecting the satellite fraction in the samples while modelling the signal. We provide a model that accounts for both the role of satellites and the differences between different

[3] http://kids.strw.leidenuniv.nl

data sets: we investigate the compatibility of the measurements in the literature within this framework. In Sec. 4 we address the behaviour of satellites at small scales. We reanalyse the G19 measurement in the context of a red/blue distinction of the galaxy population, and model the satellite alignment including both a radial and luminosity dependence. In Sec. 6 we show the predicted IA signal and illustrate the impact on cosmic shear studies. We investigate the impact of adopting a too simplistic IA model when performing cosmological analysis and address the level of bias expected for a Stage III (current generation) and a Stage IV (next generation) surveys. In Sec. 7 we draw our conclusions.

Throughout this paper we assume the MICE cosmology as our cosmological model of reference: a spatially flat ΛCDM model with $h = 0.7$, $\Omega_m = 0.25$, $\Omega_b = 0.044$, $\Omega_\Lambda = 0.75$, $n_s = 0.95$, $\sigma_8 = 0.8$. We use $\bar{\rho}_m$ as the present day mean matter density of the Universe. We provide our predictions and measurements in units of h. Absolute magnitudes are always given assuming $h = 1$.

2 MICE SIMULATION

To investigate the impact of red and satellite fractions on the IA signal, we need a realistic representation of the galaxy sample that populates a cosmic shear survey. Krause et al. (2016) has shown that one of the major sources of uncertainties in forecasting IA for future cosmic shear surveys comes from the uncertainty in the luminosity function modelling, which determines the red/blue fraction of galaxies in the analysis. In this work, we make use of the MICECATv2.0 [4] simulation (Fosalba et al. 2015) as a realisation of our Universe and select galaxies based on the typical values of redshift, magnitude and area for a Stage III survey. We use the simulations as our reference cosmic shear survey, for which we can extract all the necessary information.

MICECAT is a public catalogue, now at its second data release, created to reproduce a number of local observational constraints and it is for this reason particularly suitable for our purposes. The mock galaxy catalogue is obtained from an N-body simulation containing 7×10^{10} dark matter particles in a $(3072h^{-1}\mathrm{Mpc})^3$ comoving volume (Fosalba et al. 2015) and then populated using a hybrid implementation of Halo Occupation Distribution (HOD) and Sub-Halo Abundance Matching (SHAM) (Crocce et al. 2015; Carretero et al. 2015).

Given the importance of having robust satellite fractions per luminosity and redshift bin and a representative colour distribution for our analysis, we report here the most relevant features adopted in Carretero et al. (2015) to build the galaxy catalogue. The HOD parametrisation employed to populate the haloes is inspired by Zheng et al. (2005), with some modifications that we briefly describe here. The HOD provides the probability $P(N_\mathrm{g}|M_\mathrm{h})$ that a halo of a given mass M_h contains N_g galaxies of a certain type (central, satellite). To assign galaxies to a halo, a sharp mass-threshold is adopted, such that every halo more massive than M_min contains at least one (central) galaxy. The number of satellite galaxies follows a Poisson distribution with mean $\langle N_\mathrm{sat}\rangle = [M_\mathrm{h}/M_1]^\alpha$. The slope of the power law is chosen to be $\alpha = 1$, as constrained by observations (e.g Kravtsov et al. 2004; Zehavi et al. 2011), while the mass threshold for satellite galaxies, M_1, is modelled to be a function of M_min and the halo mass M_h. The parameters of the functions that relate M_1 to M_min are those that best reproduce the observed galaxy clustering as a function of luminosity in the SDSS (Zehavi et al. 2011). Galaxy luminosities are assigned using abundance matching, based on the observed luminosity function from Blanton et al. (2003) and Blanton et al. (2005) for the faint end. Note that by construction, satellite galaxies are forced to be fainter than 1.05 times the luminosity of their central galaxy. Colours are assigned following an approach similar to Skibba & Sheth (2009): the colour-magnitude diagram is parametrised using three Gaussians, corresponding to the red, green and blue population; the mean and standard deviations vary as a function of luminosity. The colour of a galaxy is then drawn from these distributions, taking into account its type (satellite or central). The colour-assignment process is calibrated to reproduce the clustering as a function of colour and luminosity in the SDSS (Zehavi et al. 2011). In our analysis we combine the green and blue population, isolating the red sequence with a different cut than what is reported in Carretero et al. (2015), as discussed in Section 2.1.

The second release of MICE increases the luminosity range by populating halos/groups with a fewer number of particles with respect to the v1, up to haloes composed by only two particles. Although the abundance of these small groups is not representative of the abundance of haloes at the equivalent halo mass, this is then corrected by the abundance matching.

2.1 Galaxy mocks

We generate two galaxy mocks: the first one reproduces a generic Stage III survey and is employed as our fiducial cosmic shear-like galaxy distribution. A second mock is constructed for a comparison to the results of J19 and G19 in KiDSxGAMA, and therefore is designed to reproduce the KiDSxGAMA galaxies used in their analysis. We use that mock to understand and interpret our results at small scales, where we use the measurements as input for our cosmic shear analysis. If not specified otherwise, we always refer to the Stage III mock in this work.

We select 58 485 848 galaxies from MICECAT v2, covering an area of 1049 deg^2 in a redshift range $0.1 < z < 1.3$. We impose a magnitude cut in the SDSS r−band $r < 24$. We split the sample into six redshift bins with $\Delta z = 0.2$, as shown in Fig. 1a. We correct the magnitudes to take into account the passive evolution of galaxies, as recommended in the MICE readme.

As discussed in the previous section, MICE is complete down to $M_r - 5\log(h) \sim -14$. With our selection, we are close to this limit (the faintest galaxy in our catalogue has a magnitude of $M_r - 5\log(h) = -13.4$). However, since IA is mainly affected by red galaxies, which are typically brighter than this value, even a small incompleteness should not significantly impact our results.

MICE provides colours in the filters ${}^{0.1}r$ and ${}^{0.1}g$. To be consistent with the data-set we aim to compare the mocks

[4] MICECAT v2 is publicly available at https://cosmohub.pic.es/home

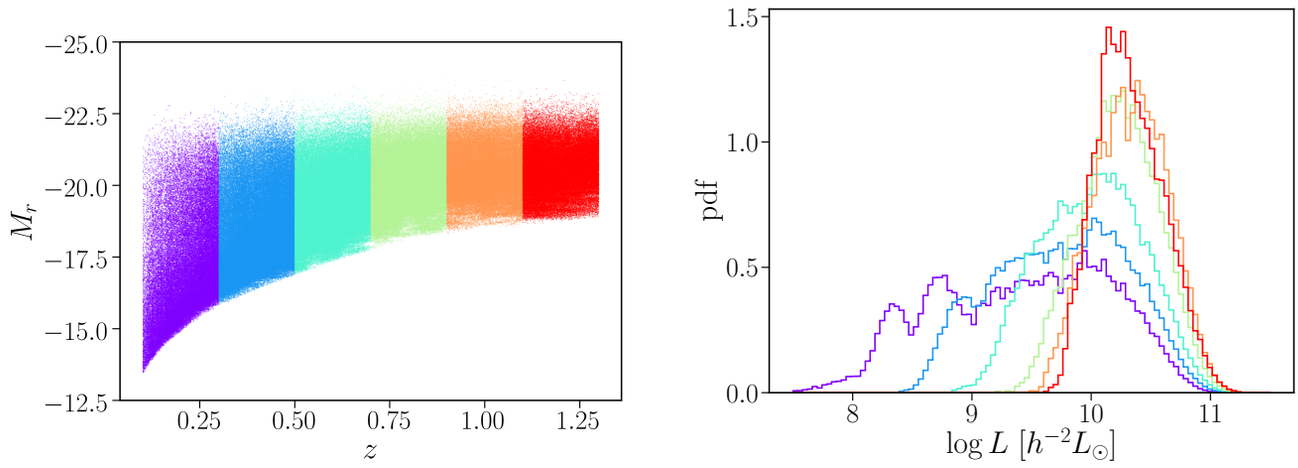

(a) (b)

Figure 1. (a): The distribution in redshift and magnitudes of the sample we select from MICE, with the imposed cut in apparent magnitude at $r < 24$. The figure illustrates the samples used in our analysis for the six redshift bins listed in Table 1. The plot shows a random selection of 1% of the galaxies in the catalogue. (b): The magnitude distribution of the red central galaxy samples for the six redshift bins, colour coded as in (a).

to, namely GAMA and the SDSS Main sample used by J19 and G19, which select their galaxies using the $g-r$ colour at $z = 0$, we correct the MICE $g-r$ colour to be at $z = 0$ (F.J. Castander, private communication). We verify that by selecting GAMA-like and SDSS-like mock galaxies from the MICE simulation, imposing the same area coverage, redshift ranges and flux-limit cut, we can reproduce the redshift and magnitude distribution of the samples, the colour-magnitude diagram and the relative galaxy fractions (Appendix A). We therefore conclude that MICE galaxies provide a realistic mock for our analysis.

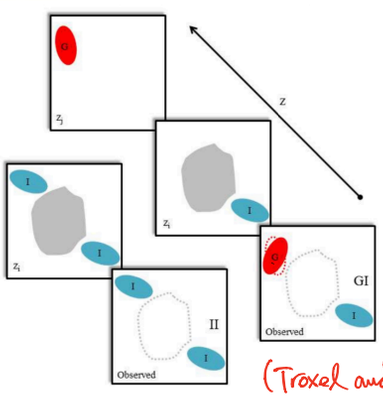

(Troxel and Ishak 2015).

0.012 repro acter redsh the f shifts to th last t highe at $g-r > 0.61-$ cut qualitatively marises the char- y sample in each d on our sample, ı low to high red- st three bins, due decreases for the f blue galaxies at

3 THE IMPACT OF SATELLITES AT LARGE SCALES

Intrinsic galaxy alignment generates two types of 2-point statistic observables that are relevant in the context of cosmic shear contamination: the correlation between the shapes of two galaxies (II) and the correlation between the gravitational shear induced by the lensing effect of a matter inhomogeneity and the intrinsic shape distorted by the same gravitational source (GI). The final observable is then given by the sum of the cosmic shear power spectrum (GG), which is the one of interest for cosmological studies, and the IA contributions, II and GI.

$P_{obs} = P_{GG} + (P_{GI} + P_{IG} + P_{II})$

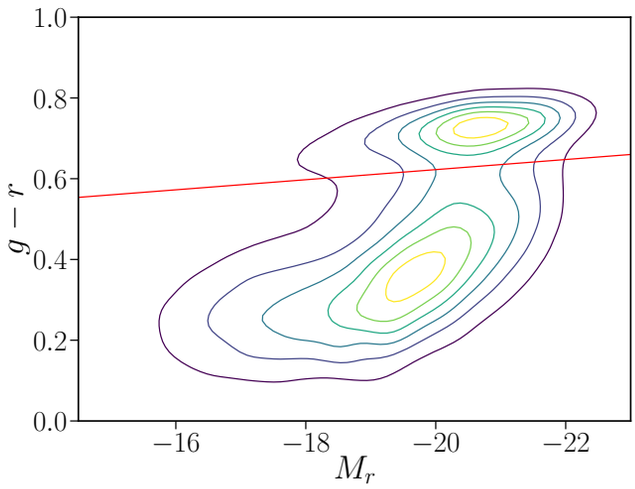

Figure 2. The colour-magnitude distribution of the sample. The red line shows the cut at $g-r > 0.61-0.0125(M_r+19)$ we employ to isolate the red sequence.

3.1 The linear alignment model

It is well established that at large scales elliptical galaxies can be modelled through the linear alignment model (Catelan et al. 2001; Hirata & Seljak 2004), which predicts the shape distortion of a galaxy to be proportional to the strength of the tidal field at the moment of its formation. In Fourier space, the matter-intrinsic power spectrum can thus be written as

$$P^{\rm LA}_{\delta I}(k,z) = A_{\rm IA} C_1 \rho_c \frac{\Omega_m}{D(z)} P^{\rm lin}_\delta, \quad (1)$$

where C_1 is a normalisation constant, $D(z)$ the linear growth factor, normalised to unity at $z = 0$, and $P^{\rm lin}_\delta$ the linear matter power spectrum. We set $C_1\rho_c = 0.0134$ based on the IA amplitude measured at low redshifts on SuperCOS-

Table 1. Properties of the five tomographic bins used in our analysis: the redshift range of each bin ($z_{\rm min}$, $z_{\rm max}$), the number of galaxies ($N_{\rm gal}$), the mean luminosity of the red central galaxies in terms of a fiducial luminosity L_0 ($\langle L_{\rm cen}^{\rm red}\rangle/L_0$), the fraction of satellites in the given bin ($f_{\rm sat}$) and the fraction of red galaxies ($f_{\rm red}$), selected as shown in figure 2. The fiducial luminosity L_0 is chosen to be the luminosity corresponding to $M_r = -22$.

Bin	$z_{\rm min}$	$z_{\rm max}$	$N_{\rm gal}$	$\langle L_{\rm cen}^{\rm red}\rangle/L_0$	$f_{\rm sat}$	$f^{\rm red}$	$f_{\rm sat}^{\rm red}$	$f_{\rm sat}^{\rm blue}$
1	0.10	0.30	7633382	0.17	0.41	0.15	0.10	0.31
2	0.30	0.50	12445504	0.24	0.37	0.22	0.14	0.23
3	0.50	0.70	12453204	0.33	0.33	0.27	0.16	0.17
4	0.70	0.90	9863462	0.48	0.28	0.28	0.15	0.13
5	0.90	1.10	8003975	0.58	0.23	0.25	0.12	0.11
6	1.10	1.30	8086321	0.55	0.22	0.26	0.13	0.09

MOS (Hirata & Seljak 2004; Bridle & King 2007). The free amplitude $A_{\rm IA}$ captures any variation with respect to this reference power spectrum. The SuperCOSMOS norm is a common choice in the literature, making the interpretation of our results and any comparison easier.

A successful modification of this theory replaces the linear matter power spectrum with the non-linear one (Bridle & King 2007), so named non-linear linear alignment (NLA). Although the theoretical motivation behind the use of the nonlinear power spectrum is relatively poor, it has been shown to fit the measurements better (for example, Joachimi et al. 2011; Singh et al. 2015; Johnston et al. 2019). To capture the IA signal at intermediate scales, we therefore use the NLA model in our analysis.

3.2 From observations to models: how satellite galaxies complicate the picture

As direct measurements of the correlation between the density field and the shear field (δI) are not possible, IA studies typically focus on the correlation between the position of a galaxy and the shape of another one, the so called gI term. At large scales, the galaxy position - shear and the matter - shear power spectra are related by the large scale bias, galaxies being tracers of the underlying matter distribution. For central galaxies, the relation between gI and δI is simply given by the linear galaxy bias, such that $P_{\rm gI}(k) = b_g\ P_{\delta{\rm I}}$

A complication arises when interpreting the gI term in the presence of satellite galaxies. Satellites tend to preferentially lie along the major axis of the central galaxy (Huang et al. 2016, J19, G19), which in turn is a proxy for the halo major axis. This anisotropic distribution of satellite positions boosts the satellite position - central shape (sc) correlation not only at small scales, but also in the two-halo regime, i.e. when correlating the shape of a central galaxy with the position of a satellite that belongs to a different halo.

In the context of contamination to lensing, however, such a boost is not expected to have the same importance. Since cosmic shear analyses only correlate shapes, the spatial segregation of satellites is not sufficient to induce a GI signal (where GI is the projected matter - shear power spectrum, i.e. the one that directly contaminate lensing), as satellites need to be coherently oriented to produce a shape correlation (for a discussion on this in simulations, see for example Chisari et al. 2015b).

The impact of the anisotropic distribution of satellites has been explored in simulations by Samuroff et al. (2019), who found a significant enhancement of the signal at small scales and a constant, redshift independent shift at large scales. They found that for an LSST-like (Stage IV) survey, in the 'pessimistic' case (see their section 5.2), this can lead to a shift in the best constrained parameters $\Delta S_8 = 1.4\sigma$, $\Delta w = 1.5\sigma$. The recent results from G19, however, show that at large scales satellite galaxies are randomly oriented, while within the halo their radial alignment is limited to the innermost galaxies. J19 also found a similar trend when looking at the projected satellite position - shape correlation and central position - shape correlation (their Fig. 7, right panels), suggesting satellites to only coherently orient their shapes in the intra halo regime. Using the same estimator as G19, $\langle\epsilon_+\rangle$, Sifón et al. (2015) found a radial alignment consistent with zero in clusters. Although every detection depends on the choice of the shape measurement algorithm employed, those results suggest that at large scales satellite alignment is a minor contributor compared to the central galaxy alignment. At small scales the picture might be significantly different: we refer the reader to Section 4 for a discussion on the contribution of satellites at small scales.

While the relative positions of satellites within the halo have a strong impact on the gI correlation, from the argument above, they are not expected to be important in the correlation between the lensed background galaxies and the intrinsically aligned galaxies in the foreground. In this regard, the anisotropic distribution of satellites within the halo complicates the translation of gI measurements to GI, so care has to be taken when adopting informative priors for IA that come from gI measurements. An analysis of this contamination is outside the scope of this paper, and we leave a full modelling of the gI term that can disentangle the two contributions to a forthcoming paper. Given the argument above, we assume that at first order satellites do not contribute to the IA signal at large scales.

3.3 A weighted linear alignment model

We have seen in the previous section that for the sake of accounting for IA contamination in cosmic shear analyses, the role played by satellites is small at large scales. In this sense, central galaxies provide a more consistent picture as they follow the linear alignment mechanism, while the contribution of satellites is mainly to add noise to the measurements. In this context, we can assume that the majority of the contamination comes from the alignment of red central

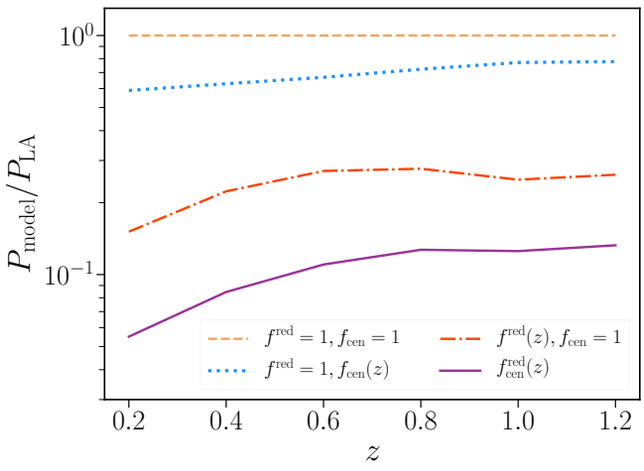

Figure 3. An illustration of the redshift dependence of the IA power spectrum at large scales (2-halo regime) due to the change of the fraction of red and satellite galaxies over the z-bins. We plot the ratio of a 'weighted' GI power spectrum and the standard LA one. We assume a constant signal with amplitude $A = 1$ (gold dashed line); incorporating the satellite fraction decreases the overall amplitude; at high redshift the fraction of satellites drops (see table 1), with a consequent increase of the signal (blue dotted line). At high redshift blue galaxies become important, suppressing the signal (red dot-dashed line). Only red central galaxies are expected to contribute to the total signal (purple solid line).

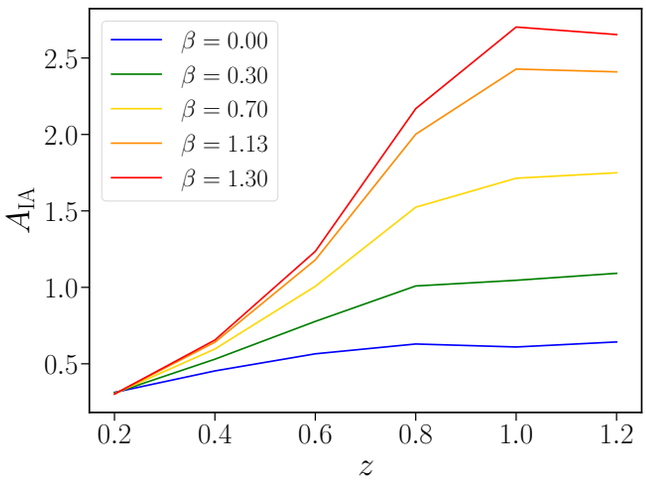

Figure 4. The IA signal for different values of the slope of the power law β (eq. 6), as predicted for our simulated Stage III survey. The observed z–dependence of the signal is only caused by the different galaxy samples that populate the z-tomographic bins.

galaxies, while blue central galaxies are expected to add a minor although still very uncertain contribution.

Assuming that to first order the modes responsible for the alignment of red and blue galaxies are uncorrelated, we can write the large-scale power spectra as:

$$P^{2h,\rm red}_{\delta \rm I}(k,z) = f^{\rm red}_{\rm cen} P^{2h,\rm red}_{\delta \rm I, cc}(k,z) + f^{\rm blue}_{\rm cen} P^{2h,\rm blue}_{\delta \rm I, cc}(k,z)\,, \quad (2)$$

$$P^{2h,\rm red}_{\rm II}(k,z) = (f^{\rm red}_{\rm cen})^2 P^{2h,\rm red}_{\rm II, cc}(k,z) + (f^{\rm blue}_{\rm cen})^2 P^{2h,\rm blue}_{\rm II, cc}(k,z)\,, \quad (3)$$

where we have introduced the superscript $2h$ to indicate that these power spectra describe the alignment in the two-halo regime, i.e. for galaxies that do not belong to the same halo (large scale alignment). Similarly, the subscript cc indicates that the correlation only involves central galaxies. $f^{\rm red/blue}_{\rm cen}$ is the fraction of central galaxies in the red/blue sample, and we have $f^{\rm blue} = 1 - f^{\rm red}$, $f^{\rm red}_{\rm cen} + f^{\rm blue}_{\rm cen} = f_{\rm cen}$ of the entire sample. Note that these re-scalings are required only when the amplitude of the signal is measured on a central-dominated galaxy sample.

Figure 3 shows the competing effect of blue and satellite galaxies in suppressing the signal at high and low redshift respectively. Assuming a constant IA signal with amplitude $A = 1$, it illustrates how the change of the red and the satellite fractions across the tomographic bins can affect the IA amplitude at large scales. The purple solid line shows the total amplitude (equation 2): the evolution of the fraction of red central galaxies induces a sample-dependent redshift evolution of the *measured* IA signal. Weighting the signal by the (red) central galaxies only significantly reduces the amplitude of the predicted IA.

3.4 Luminosity dependence of the IA signal

A luminosity dependence of the IA signal has been explored in the context of the large scale alignment of elliptical galaxies in a number of works (Hirata et al. 2007; Joachimi et al. 2011; Singh et al. 2015, J19). A common approach to model this is to follow the parametrisation in Joachimi et al. (2011):

$$P^{2h}_{\rm GI}(k,z,L) = P^{2h}_{\rm GI}(k,z)\left(\frac{L}{L_0}\right)^{\beta}, \quad (4)$$

$$P^{2h}_{\rm II}(k,z,L) = P^{2h}_{\rm II}(k,z)\left(\frac{L}{L_0}\right)^{2\beta}, \quad (5)$$

where L_0 is a pivot luminosity, assumed to correspond to $M_r = -22$.

The value of β is, however, being debated: while Joachimi et al. (2011) in the MegaZ-LRG + SDSS LRG + L4 + L3 samples - hereafter simply MegaZ - and Singh et al. (2015) in LOWZ find similar values ($A_{\rm MegaZ} = 5.76^{+0.60}_{-0.62}$, $\beta_{\rm MegaZ} = 1.13^{+0.25}_{-0.27}$; $A_{\rm LOWZ} = 4.5^{+0.6}_{-0.6}$, $\beta_{\rm LOWZ} = 1.27^{+0.27}_{-0.27}$), J19, fitting to GAMA + SDSS Main sample galaxies, find $A_{\rm G+S} = 3.40^{+0.59}_{-0.56}$ and $\beta = 0.18^{+0.20}_{-0.22}$. As pointed out by J19, the galaxies employed in their study contain a larger fraction of satellites compared to the MegaZ and LOWZ samples; the way this can impact the luminosity dependence is, however, non-trivial.

Since cosmic shear surveys span a range in luminosity much broader than what is used in those analyses, the impact of a luminosity dependence can be important in modulating the signal over the redshift bins. Different values of β can lead to a significantly different contamination of lensing measurements (Chisari et al. 2015a). To illustrate this, we consider the case of different values of β and normalise the amplitude such that all of the curves pass through the measured amplitude $A = 4.5$ of the LOWZ galaxies at the mean redshift of the sample, $z = 0.21$ (Fig. 4). Even in the case of no luminosity scaling at all, the increasing luminosity of the

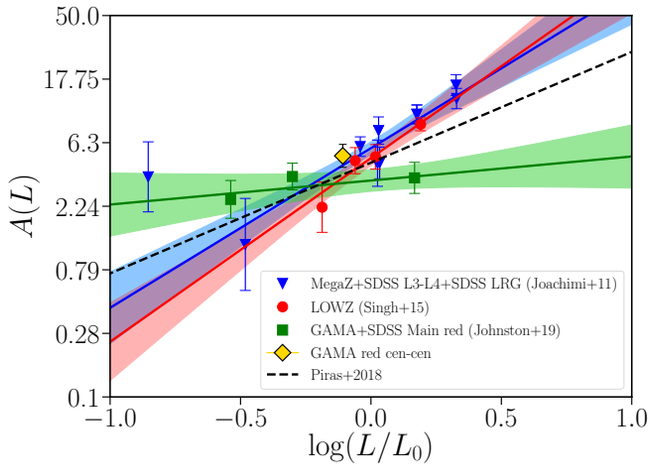

Figure 5. The different luminosity scaling predicted by MegaZ (blue line), LOWZ (red line) and GAMA+SDSS Main (green line) bestfit curves, together with the three individual sample fits in J19 (green squares). The middle and right point corresponds to the Z1 and Z2 samples. The yellow diamond indicates our best fit amplitude of the position - shear, central - central correlation.

galaxies that populate the bins and the consequent drop of the number of satellites induce a redshift dependence of the IA signal, which has to be included in the lensing analysis. If β is non-zero, such a redshift dependence is significantly amplified, with a much larger amplitude at high redshift, where the sample is dominated by brighter galaxies. To evaluate the average luminosity scaling $\langle (L/L_0)^\beta \rangle$ for our comic shear-like sample, we integrate over the pdf shown in Fig. 1b.

Since the impact of an evolving signal would not be captured by a fixed IA amplitude, as often done in weak lensing analyses, it is important to understand whether a luminosity dependence exists in the data. We point out that since the luminosity dependence has only been observed in the context of red galaxy alignment, in the rest of this section we limit the discussion to the red population only.

3.4.1 *The case of GAMA galaxies*

The GAMA survey is a highly complete spectroscopic survey (>98 per cent in the r-band down to $r = 19.8$), which overlaps with $\sim$ 180 deg^2 of KiDS data. The KiDS data provide high-quality galaxy images, from which Georgiou et al. (2019b) has measured the shapes with the DEIMOS (DEconvo-lution In MOments Space) shape algorithm (Melchior et al. 2011). This shape catalogue is employed in J19 and G19 for their IA studies.

J19's fit of β is obtained using three samples of red galaxies: the SDSS Main, and two samples from the GAMA, cut at $z = 0.26$ in two equally populated redshift bins, Z1 and Z2. The individual fits to these samples are shown in Fig. 5 with green square markers. In this section, we explore whether the discrepancy on the value of β can be due to the presence of satellites in their samples. We focus on the GAMA samples only, for which we can obtain an estimate of the fraction of satellites through the GAMA Group Catalogue[5].

As discussed in Section 3, satellite galaxies tend to randomly orient their shapes at large scales, not contributing to a *shear* signal. At the same time, they preferentially lie along the major axis of their central galaxy, contributing to the satellite position - central shape correlation. In a halo model fashion, we can think of these contributions to sum up linearly, weighted by the fraction of galaxies that contribute to each term, together yielding the final signal that we measure.

J19 shows that the *sc* contribution is non-negligible, being as large as the typical central-central alignment at large scale (left panels of their Fig. 7). The individual fits to the alignment signals of the Z1 and Z2 samples show roughly a similar amplitude ($A_{Z1} = 3.63^{+0.79}_{-0.79}$, $A_{Z1} = 3.55^{+0.90}_{-0.82}$) corresponding to galaxies of different luminosity ($\langle L/L_0 \rangle_{Z1} = 0.50$, $\langle L/L_0 \rangle_{Z2} = 1.47$), compatible with their finding of no luminosity dependence. However, at low redshift the fraction of satellite galaxies in their red population is roughly 0.35, meaning that the amplitude of the red sample in Z1 is significantly affected by the *sc* term (*cs* and *ss* do not contribute at large scales). The fraction of satellites in the sample slightly decreases in the second redshift bin ($f_{sat} \sim 0.28$). If we assume that the luminosity dependence is a feature related to the shape orientation, which is instead unrelated to galaxy position, this can partially explain the discordance of their result (note that a simple re-weighting of these signals is not possible as satellites also change the luminosity of the sample).

To confirm our intuition, we measure the IA amplitude of the red central sample only in GAMA (*cc* correlation). The mean luminosity of this sample is $\langle L/L_0 \rangle = 0.78$, for which we find a best fit amplitude $A_{\mathrm{GAMA},cc} = 5.08^{+0.97}_{-0.95}$, with a reduced $\chi^2 = 2.0$ ($N_{\mathrm{dof}} = 4$). This measurement agrees with the curve predicted by MegaZ and LOWZ, which would correspond to 4.97 ± 0.24 at that given luminosity (assuming MegaZ parameters), as illustrated in Fig. 5. Our new measurement is displayed as the yellow diamond, while the predicted best fit luminosity dependent IA amplitude measured by MegaZ and LOWZ are shown as blue and red curves, respectively. Note that the MegaZ best fit curve also includes a $z-$dependent power law that was poorly constrained in that work. We do not include it here, as recent studies have not found evidence for an intrinsic z-dependence of alignment strength, so the curve reported in Fig. 5 is only the luminosity dependent part of their fit.

3.4.2 *A central-only luminosity dependent signal*

Limiting the luminosity dependence to central galaxies finds a natural theoretical frame in the context of the linear alignment mechanism, where the intrinsic shear power spectrum can be expressed as a power of the mass of the hosting halo (Piras et al. 2018). This can in turn be related to the luminosity of its central galaxy. Figure 5 shows the relation found in Piras et al. (2018) when fitting the mass dependence of the IA signal for the LOWZ, MegaZ-LRG, SDSS LRG and the redMaPPer galaxy clusters in van Uitert &

[5] http://www.gama-survey.org

Joachimi (2017). The latter measured the IA signal with a different estimator, which might be responsible for the overall shallower luminosity dependence constrained when the cluster measurements are included. To convert the mass dependence to a luminosity dependence, we used an average of the mass-to-light relation for LOWZ and CMASS galaxies from van Uitert et al. (2015).

Given our results for the GAMA sample and the converging results for MegaZ and LOWZ, which sample similar galaxies, we suggest that red central galaxies follow the luminosity scaling detected in Joachimi et al. (2011) and Singh et al. (2015) and the final power spectra should be weighted by the fraction of galaxies that generate such a signal, i.e. the red central galaxies:

$$P^{\rm red}_{\delta \rm I}(k,z,L) = f^{\rm red}_{\rm cen} P_{\delta \rm I}(k,z) \left\langle \left(\frac{L^{\rm red}_{\rm cen}}{L_0} \right)^{\beta} \right\rangle \quad (6)$$

and

$$P^{\rm red}_{\rm II}(k,z,L) = (f^{\rm red}_{\rm cen})^2 P_{\rm II}(k,z) \left\langle \left(\frac{L^{\rm red}_{\rm cen}}{L_0} \right)^{2\beta} \right\rangle. \quad (7)$$

Although the alignment of central galaxies with luminosities $L > L_0$ seems to be captured better by the LOWZ/MegaZ best fit curve, Fig. 5 shows that the alignment of low luminosity galaxies is still poorly constrained, such that the exact value of β is still hard to determine in that range with current uncertainties. We also caution that LOWZ and MegaZ are not pure central galaxy samples (for example, LOWZ has roughly a fraction 11% of satellites, see Singh et al. (2015), Sec. 3.3), which also contaminates the results, particularly in the faint end of the curve.

3.5 Colour dependence

A key aspect of our approach is that we weight the alignment signal by the fraction of galaxies that contributes to that specific amplitude. We have seen that the IA alignment is strongly morphology dependent: this implies that the weighting by the red fraction plays a significant role in the prediction of the final signal. The different measurements compared in the previous section have been measured on samples selected with different red cuts. However, Singh et al. (2015) has explored the dependence of the IA signal on colour, finding no evidence for a colour-dependence in the data. Since J19 provide IA amplitudes for both the red and blue samples, and we have shown that their measurements agree with the results in MegaZ and LOWZ once restricting the analysis to the central sample only, we adopt J19 amplitude for the blue population and consistently apply a red cut similar to the one in their work (see Sec. 2.1).

4 THE IMPACT OF SATELLITES AT SMALL SCALES

To model the impact of satellite alignment at small scales, we revisit the halo model formalism by SB10 to take into account new observational results. The spherical halo approximation should capture most of the small-scale GI signal. As discussed in Sec. 3, the anisotropic distribution of satellites boosts the signal of the gI correlation, so a spherical

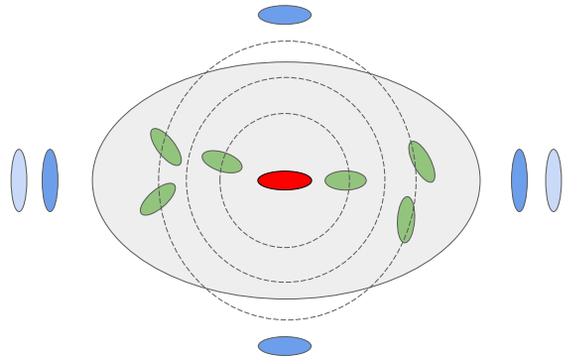

Figure 6. A cartoon showing the current picture of satellite alignment provided by observations. Satellite galaxies (green ellipses) tend to preferentially segregate along the direction of the central galaxy (red ellipse) major axis; the closest satellites to the centre of the halo show a preferential alignment in the direction of the central galaxy major axis. The source galaxies (blue ellipses) are tangentially aligned with respect to the halo shape, resulting in an opposite alignment with respect to the aligned satellites and the central galaxy. We can expect source galaxies to be lensed more along the halo major axis, due to the excess of matter in that direction. The dotted circles illustrate the way a spherical halo model can describe this alignment signal.

model would underestimate w_{g+}. How it propagates exactly in the context of the GI contamination is not trivial. The satellite segregation along the central galaxy major axis is expected to source a large 1-halo satellite position - satellite shear correlation, confirmed in J19, but also of an opposite satellite-satellite II term, for which we do not have any observational measurement. Moreover, if only the innermost satellites are aligned in the direction of the central galaxy, as observed in G19, the impact on GI should be significantly reduced compared to gI. For an illustration of these terms, see the cartoon in Fig. 6. Although further study is needed, we use the spherical halo model formalism because we expect it to capture the leading contribution, providing a fair sense of the amplitude of the satellite alignment.

4.1 The halo model formalism for satellite alignment

Following SB10 we adopt an effective radial satellite alignment and describe galaxy orientations inside the halo through the stick approximation. In this approximation, the two minor axes of the elliptical galaxy have equal lengths on average and the length and the orientation of the stick correspond to those of the galaxy major axis.

Defining a Cartesian reference system centred on the halo and with the $z-$axis along the line of sight, the position of a satellite galaxy inside the halo is identified by the vector $\mathbf{r} = (r, \theta, \phi)$. The orientation of the satellite major axis can then be expressed through the unit vector

$$\hat{e} = (\sin\theta_e \cos\phi_e, \sin\theta_e \sin\phi_e, \cos\phi_e), \quad (8)$$

where θ_e and ϕ_e are, respectively, the polar and azimuthal angles that the satellite major axis forms with the radial vector $\mathbf{r}$.

In principle, we expect satellite galaxies to follow a dis-

tribution of angles between their major axes $\hat{e}$ and the radial vector $\mathbf{r}$. However, SB10 showed that the main effect of including this term is simply to reduce the amplitude of the correlation functions with respect to the case of perfect radial alignment, independently of the halo mass. Thus, we can simply consider the case of perfect radial alignment, absorbing any misalignment into the amplitude of the intrinsic alignment signal. In this case, $\theta_e = \theta$ and $\phi_e = \phi$. In a sense, the perfect radial alignment configuration can be considered as an effective description: we can only measure the tendency of galaxies to point in a certain direction, so the length of the sticks - which determines the amplitude of the signal - quantifies the amplitude of the misalignment angle. This provides a direct map between the formalism of the stick model and the measured alignment $|\epsilon|\langle\cos(2\phi)\rangle$, where $|\epsilon|$ is the modulus of the ellipticity and ϕ is the misalignment angle.

Calling $\bar{\gamma}$ the length of the stick, and assuming the alignment to be a function of the distance to the halo centre and the mass of the halo, it follows that (SB10)

$$\gamma^I(\mathbf{r}, M, c) = \bar{\gamma}(r, M, c)\sin\theta e^{i2\phi}. \tag{9}$$

Here, $\gamma(r, M)\sin\theta$ is the observed length of the stick, corresponding to the projection of the major axis along the line of sight. In principle, this quantity can also depend on the halo concentration, but we assume a deterministic relation between mass and concentration (see also Sec. 5) and so we omit such dependence here.

Since we only measure the IA signal at galaxy locations, it is necessary to introduce a density weighting in the model (Hirata & Seljak 2004), $\tilde{\gamma}^I = \gamma^I(1+\delta_g)$. This is particularly important at small scales, where the galaxy density contrast is large. Following SB10, we weight the 3D projected ellipticity by the number of galaxies inside the halo, N_g and the normalised matter density profile $u(\mathbf{r}|M) = \rho(r|M)/M$:

$$\tilde{\gamma}^I_{1-\rm halo}(\mathbf{r}, M) = \bar{\gamma}^I(r, M)\sin\theta e^{2i\phi} N_g u(\mathbf{r}|M), \tag{10}$$

where we identify the density-weighted shear with a tilde (Hirata & Seljak 2004, SB10).

Having defined the density-weighted ellipticity $\tilde{\gamma}^I$ for a given halo, we can construct a continuous intrinsic ellipticity field by summing up the contributions from each individual halo i, in the usual halo model fashion:

$$\begin{aligned}\tilde{\gamma}^I_s(\mathbf{r}) &= \frac{1}{\bar{n}_g}\sum_i \gamma^I(\mathbf{r}-\mathbf{r_i}, M_i)N_{g,i}u(\mathbf{r}-\mathbf{r_i}, M_i)\\ &= \sum_i \int \mathrm{d}M \int \mathrm{d}^3r'\ \delta_D(M-M_i)\delta^{(3)}_D(\mathbf{r}-\mathbf{r_i})\frac{N_{g,i}}{\bar{n}_g}\\ &\quad\times\gamma^I(\mathbf{r}-\mathbf{r}', M)u(\mathbf{r}-\mathbf{r}', M),\end{aligned}$$

where $\bar{n}_g$ is the galaxy number density per unit of volume, which is a function of redshift. The subscript s indicates that this density weighted shear only refers to satellites.

We calculate the correlation functions of interest for IA by correlating $\tilde{\gamma}^I_s(\mathbf{r})$ with itself and with the matter density contrast δ_m. In Fourier space, the E and B modes of the IA are defined as

$$\tilde{\gamma}^I_E(\mathbf{k}) = \cos(2\phi_k)\tilde{\gamma}^I_1(\mathbf{k}) + \sin(2\phi_k)\tilde{\gamma}^I_2(\mathbf{k}) \tag{11}$$

$$\tilde{\gamma}^I_B(\mathbf{k}) = \sin(2\phi_k)\tilde{\gamma}^I_1(\mathbf{k}) + \cos(2\phi_k)\tilde{\gamma}^I_2(\mathbf{k})\,, \tag{12}$$

where

$$\tilde{\gamma}^I(\mathbf{k}, M) \equiv \int \mathrm{d}^3\mathbf{r}\ \tilde{\gamma}^I_j(\mathbf{r}, M)\mathrm{e}^{i\mathbf{k}\cdot\mathbf{r}}. \tag{13}$$

is the Fourier transform of the complex density-weighted shear, with $j = 1, 2$ being the two components. Thus,

$$\langle\tilde{\gamma}^{I*}_E(\mathbf{k}, z)\tilde{\gamma}^I_E(\mathbf{k}', z)\rangle = (2\pi)^3\delta^{(3)}_D(\mathbf{k}-\mathbf{k}')P^{EE}_{\tilde{\gamma}^I}(\mathbf{k}, z). \tag{14}$$

and

$$\langle\delta^*(\mathbf{k}, z)\tilde{\gamma}^I_E(\mathbf{k}', z)\rangle = (2\pi)^3\delta^{(3)}_D(\mathbf{k}-\mathbf{k}')P_{\delta,\tilde{\gamma}^I}(\mathbf{k}, z) \tag{15}$$

Without loss of generality, we can rotate our reference system such that $\gamma^I_1 = \gamma^I_+$, where γ^I_+ is the tangential component of the shear. This corresponds to fixing $\phi_k = 0$ in equations 11 and 12, transforming EE into II.

For computational reasons, it is convenient to separate the radially dependent part of the density-weighted shear, which is affected by the Fourier transform, from the terms that are only mass dependent. We then define:

$$\hat{\gamma}^I_s(\mathbf{k}, M) \equiv \mathcal{F}\left(\gamma^I(\mathbf{r}, M)\ u(\mathbf{r}, M)\right). \tag{16}$$

We now have the ingredients to compute all of the possible IA power spectra. SB10 have demonstrated that at small scales, the II satellite-satellite power spectrum dominates over all of the other II terms (see their Fig. 4); similarly, the δI power spectrum is dominated by the satellite-matter term. Thus, we focus on those terms only, which can be written as

$$P^s_{\delta\rm I,1h}(\mathbf{k}, z) = \int \mathrm{d}M\ n(M)\frac{M}{\bar{\rho}_m}f_s(z)\frac{\langle N_s|M\rangle}{\bar{n}_s(z)}|\hat{\gamma}^I_s(\mathbf{k}|M)|u(k, M) \tag{17}$$

and

$$P^{ss}_{\rm II,1h}(\mathbf{k}, z) = \int \mathrm{d}M\ n(M)f^2_s(z)\frac{\langle N_s(N_s-1)|M\rangle}{\bar{n}^2_s(z)}|\hat{\gamma}^I_s(\mathbf{k}|M)|^2 \tag{18}$$

where $n(M)$ is the halo mass function, $f_s(z)$ is the fraction of satellite galaxies as a function of redshift and $\langle N_s|M\rangle$ is the halo occupation distribution of satellite galaxies.

The power spectra in equations 14-15 are functions of (k, θ_k). However, θ_k only modulates the strength of the amplitude of the signal. In the rest of the paper, we decide to fix $\theta_k = \pi/2$ (Limber approximation, for a more detailed discussion of the angular dependence of the power spectra, see Appendix B).

4.2 Radial dependent satellite alignment

We use the mean radial alignment signal $\langle\epsilon_+\rangle$ measured in G19 to model the satellite alignment in Eq. 10, $\bar{\gamma}(\mathbf{r}, M)$. They measured a satellite alignment in bins of projected distance of the satellite from the group's brightest galaxy, $r_{\rm sat}/r_{200}$ and found a radially dependent signal. It is well-fitted by a power law of the form $\langle\epsilon_+\rangle = A(r_{\rm sat}/r_{200})^b$. The slope is chosen to be fixed at $b = -2$ and the amplitude is fit for the different galaxy samples. G19 do not detect any mass dependence, so we do not include it in our parametrisation.

In order to prevent unphysiscal behaviour at very small scales, we adopt a piecewise function of the form

$$\bar{\gamma}(r) = \begin{cases} a_{1h}\left(\frac{0.06}{r_{\rm vir}}\right)^b, & \text{if } r < 0.06\ \text{Mpc}/h \\ a_{1h}\left(\frac{r}{r_{\rm vir}}\right)^b, & \text{if } r > 0.06\ \text{Mpc}/h\,, \end{cases} \tag{19}$$

where a_{1h} is the amplitude of the power law. We further impose that $\bar{\gamma}(r)$ never exceeds 0.3, which corresponds to a perfect alignment. We choose to set $r = 0.06$ Mpc/h based on the minimum angular separation for a shape measurement, which we assume to be $\theta_{\rm max} = 4$ arcsec for a ground-based telescope. At high redshifts, the largest separation that can be resolved is around 60 kpc/h. At low redshifts, the spatial resolution is much smaller, but the light coming from the central galaxy, in particular for the most massive ones, can contaminate the measurements up to this scale (Sifón et al. 2018). A cut at 0.06 Mpc/h slightly suppresses the signal of the low mass galaxies, for which the satellite alignment is expected to be small. A space-based telescope such as *Euclid* will be able to resolve objects down to a smaller separation, but the physical extent and the contamination from the central galaxy still impose a truncation at small scales. Reducing the transition value increases the amplitude of the signal, as satellites get more and more aligned as we approach the centre of the group/cluster. We experimented with different values of the truncation parameter and we find the impact to be subdominant with respect to the other source of uncertainties considered in this paper. However, future lensing studies that aim to include very small separations have to cope with an increasing IA contamination, in a regime where we do not have observations to properly calibrate its impact.

Since we need to provide a 3D shear to the model, we investigate how a radial dependence in 3D transforms when projected along the line of sight. We select 54 460 haloes from MICE, containing more than 5 satellites each, and assign to each satellite a 3D shear $\bar{\gamma}(r)$ in the form of a power law. Using the position of the galaxy within the halo to assign the polar angle θ, we first project the individual galaxy shears and then measure the average signal in bins of projected separation $r_{\rm sat}/r_{200}$. We divide our sample in 25 groups, randomly assigning the haloes to each group, and repeated the measurement of the projected signal for each group. We find that the slope of the power law is weakly reduced when projecting to 2D (from -2 to -1.8), while the amplitude is reduced from 1 to 0.7. Since the change in the slope is not large and considering that G19 do not fit for it, we decided to not modify the functional form of the satellite alignment in our calculation. We have also tested that modifying the slope of the power law in G19 in the range $b \in [-3, -1.5]$ still provides a good fit to their data points. Given the lack of stringent constraints on the slope of the power law, there are no motivations to modify it in 3D, and we assume $b = -2$ as in G19.

As for the large scale signal, we distinguish between the alignment of red and blue satellites, for which G19 find a different amplitudes.

4.3 Luminosity dependence of the satellite galaxy alignment

In the spirit of including any observational insights into our model, we focus here on the luminosity dependence of satellites. This was detected in Huang et al. (2018) in the SDSS redMaPPer galaxies but not confirmed by G19 in galaxy groups. The same dependence was explored in clusters by (Sifón et al. 2015), who did not find any evident trend with the given S/N.

Addressing whether a luminosity dependence of satellites exists is particularly important for the IA contamination of the lensing signal in the low redshift bins, where the satellite population is more abundant and spans a large range in luminosities. In particular, the lowest redshift bins of a typical lensing survey do not reflect the satellite population employed in G19, containing a larger fraction of faint blue satellites, while their sample peaks at $M_r - 22$ and has an equivalent fraction of red and blue satellites. If faint satellites are characterised by a different alignment behaviour with respect to the bright ones, extrapolating their findings might largely overestimate the IA impact on such bins.

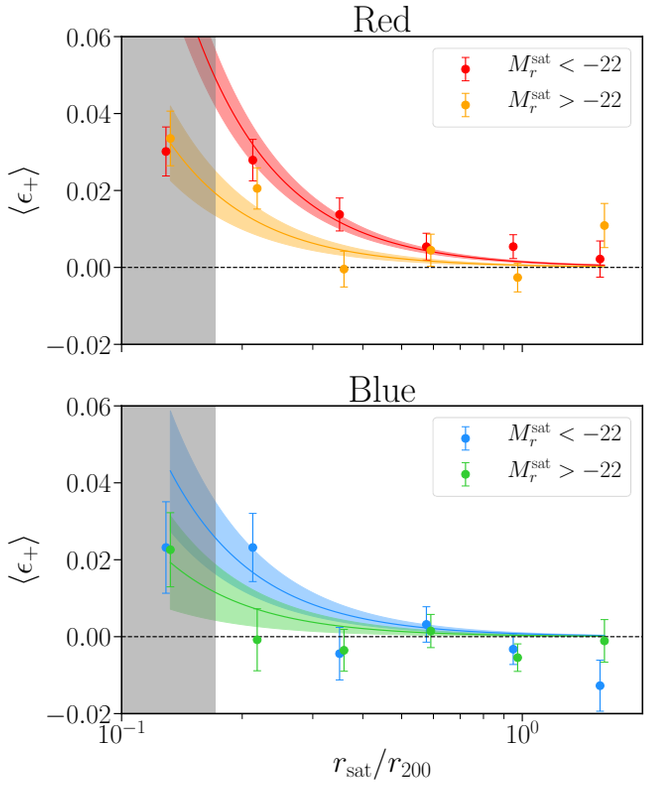

Figure 7. Mean tangential ellipticity components versus satellite projected distance from the brightest galaxy in the group, for the galaxy sample in G19. We separately consider the red (top panel) and blue (bottom panel) sample. We jointly fit the luminosity and radial dependence for each of the two samples, as in equation 20. Our best fit is on top of the data points, with the $1-\sigma$ uncertainty on the fit.

We focus on the SDSS-redMaPPer and GAMA+KiDS analyses here. Huang et al. (2018) observed that when using the re-Gaussianization shape algorithm, the satellites with ${}^{0.1}M_r < -21$, located closer to central galaxies, show a more prominent signal. Since the redMaPPer algorithm selects luminous red galaxies, one of the major differences between the galaxy samples used in the two studies is the colour of the satellites. G19 investigate the luminosity dependence only for the full sample, while Huang et al. (2018) focus on the red population only.

We re-analyse the galaxies in G19, looking for a luminosity scaling of the signal for the two separate cases of red and blue galaxies. We select red galaxies imposing the same cut as G19. We split the samples into two bins, cutting at $M_r = -22$ to ensure that the two bins have a comparable

number of galaxies. We detect a luminosity dependence for both the red and blue sample. As before, we fit a power law with fixed index $b = -2$. Our results are summarised in Table 2. Following G19, we do not include the first radial bin in our fits, since the light from the brightest galaxy of the group biases the shapes.

Although the signal-to-noise ratio does not allow for a definitive constraint on the luminosity dependence of the satellite alignment, we can draw the following conclusions: the faint blue satellites do not show any alignment signal, while the bright sample shows an alignment signal only for the innermost radial bin. The red satellites show a more prominent signal for both the faint and the bright samples. While the bright sample of the blue and the red satellites are still consistent with each other within the error bars, what drives the main difference in the red and blue satellite alignment is the behaviour of the faint bin.

To model the luminosity dependence, we decide to follow the parametrisation adopted for the red central galaxies, a power law in L/L_0, where L is now the luminosity of the satellite sample under consideration and L_0 is the pivot luminosity, corresponding to a magnitude of $M_r = -22$. We perform a joint fit of the radial and luminosity dependence for the red and blue sample separately, assuming the functional form:

$$\bar{\gamma}_{\rm red/blue}(r, L) = a_{1h} \left(\frac{L_{\rm red/blue}}{L_0}\right)^{\zeta} \left(\frac{r_{\rm sat}}{r_{\rm vir}}\right)^{b} . \quad (20)$$

As for the rest of the analysis, we do not fit for b, which is chosen to be $b = -2$. Table 2 reports our best fit values of a_{1h} and ζ for the two samples, and Fig. 7 shows our best fit curves on top of the data points.

5 HALO MODEL SETUP

To inform our model about the properties of the galaxy sample for which we predict the IA signal, we extract the HODs of central and satellites from our Stage III survey mock. We checked that this procedure gives us number densities of galaxies that match those measured in the simulations in redshift bins.

We define dark matter haloes as spheres with an average density of $200\bar{\rho}_m$. The mass of the haloes provided by MICE is based on the Friends-of-Friends (FoF) algorithm. The two definitions slightly differ from each other, in particular at high redshifts. We employ MICE masses only when computing the HODs, which enter in the small scales of the model. Those scales are important at low redshift only, so this mass-definition discrepancy is expected to not have a major impact for our analysis. This is further confirmed by the fact that we can recover compatible measured galaxy number densities within our halo model setup. In the following, we always use the M_{200} definition.

We assume that dark matter haloes follow the Navarro-Frenk-White distribution (Navarro et al. 1996), with a concentration-mass relation from Duffy et al. (2008) and that satellite galaxies are spatially unbiased with respect to the dark matter particles[6]. For the halo mass function and for the halo bias function we adopt the functional forms from Tinker et al. (2010). For the implementation of the former we make use of the public available python package HMF[7] (Murray 2014).

The total IA power spectra are given by the sum of the introduced contributions introduced in Sec. 3 eq. 6-7, describing the behaviour at large scales (2h regime), and at small scales, presented in Sec. 4, eq. 17-18. When evaluating the mass integrals we consider masses in the range $[10^{11.3}, 10^{15.5}]M_\odot/h$ to match the observed one in our mocks.

For the red sample, we assume a large-scale amplitude $A_{\rm red} = 5.33 \pm 0.6$ and a luminosity dependence with slope $\beta = 1.2 \pm 0.4$, given by the weighted mean of LOWZ and MegaZ best fit A_0 and β. For the blue galaxy alignment at large scales, we refer to the best fit amplitude in J19, who found $A_{\rm blue} = 0.21 \pm 0.37$[8].

For the satellite alignment we consider a combined radial and luminosity dependence, as discussed in Sec. 4.3. We de-project the signal in the same way as in Sec. 4.2, so that our final signal is in terms of r rather than the projected separation $r_{\rm sat}$. The radial dependence is described by equation 19. Note that in the case of the luminosity dependence, L is the mean luminosity of the red/blue satellites for each redshift tomographic bin. The final parameters are summarised in Table 3, where we also include the effect of the increase in the amplitude from the 2D to 3D power law.

6 RESULTS

Figures 8 and 9 show our predictions for the IA power spectra, based on the best fit values for the input parameters, including their 1σ uncertainties. The one-halo IA parameters $a_{\rm 1h}$ and ζ are modelled as a multivariate Gaussian with the covariance matrix computed in the fitting procedure outlined in Sec. 4.3. Since we do not have information on the covariance matrix between the parameters $A_{\rm IA}, \beta$, we assume that they follow uncorrelated Gaussian distributions centred on the best fit values and with standard deviation given by the 1σ uncertainties. We then draw 300 Monte Carlo realisations of the model, and we derive the lower and upper uncertainties using, respectively, the 16th and the 84th percentiles of the resulting distributions. The uncertainty on the IA parameters comes from the best fit on w_{g+} measurements; in the case of blue galaxy alignment, the lower limit of the IA amplitude is negative, and since this value enters squared in the II power spectrum, we can only infer the upper bounds of this quantity. For this reason, we decided to set the lower bound of the II power spectrum of blue galaxies to zero at large scales.

At low redshift and small scales, we find a larger signal that decreases as the redshifts increase, due to the drop of satellite galaxies at high redshifts imposed by the flux limit. The opposite happens for the large scales, where we

[6] We do not provide galaxy positions within the halo as implemented in MICE, but only the mean halo occupation, N_g given the mass of the halo.

[7] https://github.com/steven-murray/hmf

[8] We decided to use J19 best fit amplitude for the blue sample as input parameter for the IA signal of the central blue galaxies only. This is motivated by the fact that our sample is significantly fainter than the one used in J19 and we have seen that faint blue satellites to not show any alignment signal (Sec. 4.3).

δ: matter overdensity
g: galaxy overdensity.
γ: shear.
key plots.

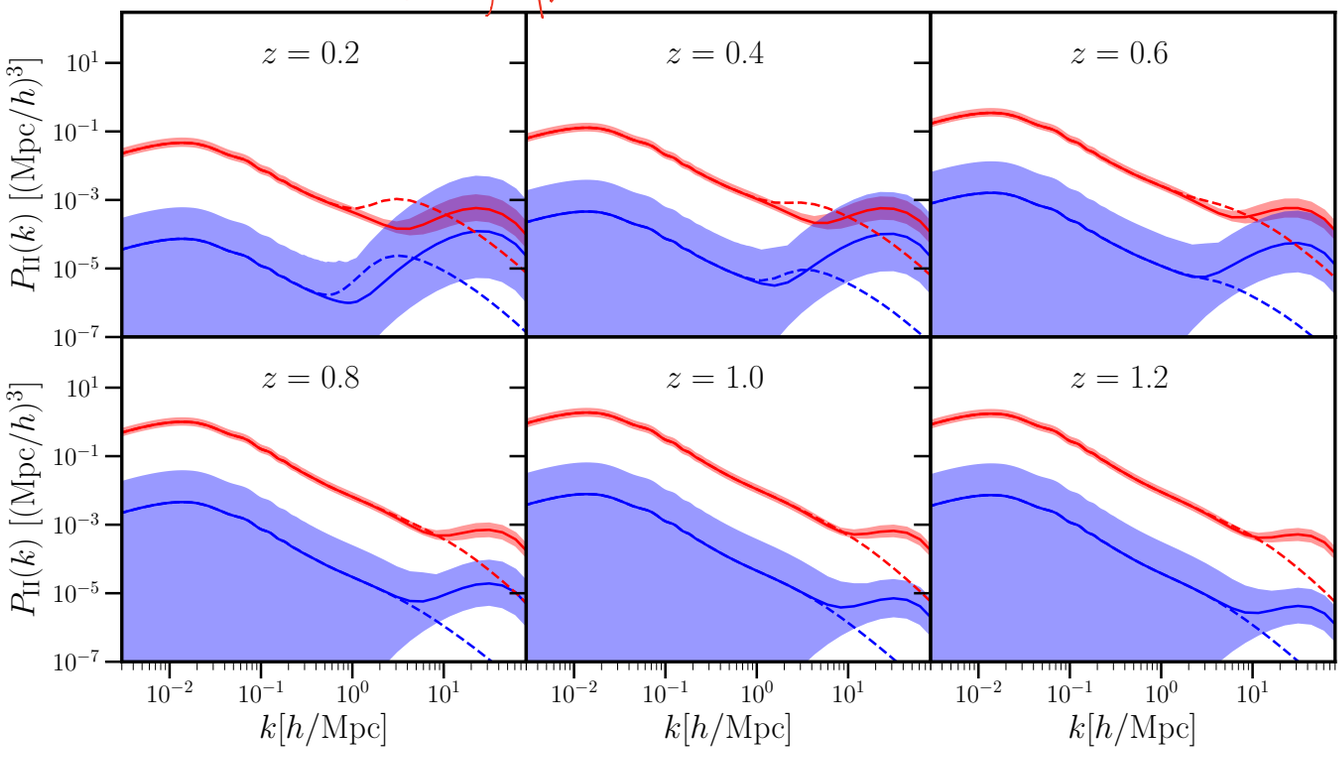

Figure 8. The intrinsic-intrinsic power spectrum for the six redshift bins considered in our analysis. The red (blue) solid line indicates our prediction for the power spectrum of the red (blue) galaxies, assuming a power law luminosity dependence (eq. 7 and 20), given the uncertainties in the best fit amplitudes (shaded area). The 1-halo amplitudes are re-scaled as described in Sec. 4.2. The dashed lines show the predictions for the case of no radial dependence for the satellite alignment signal.

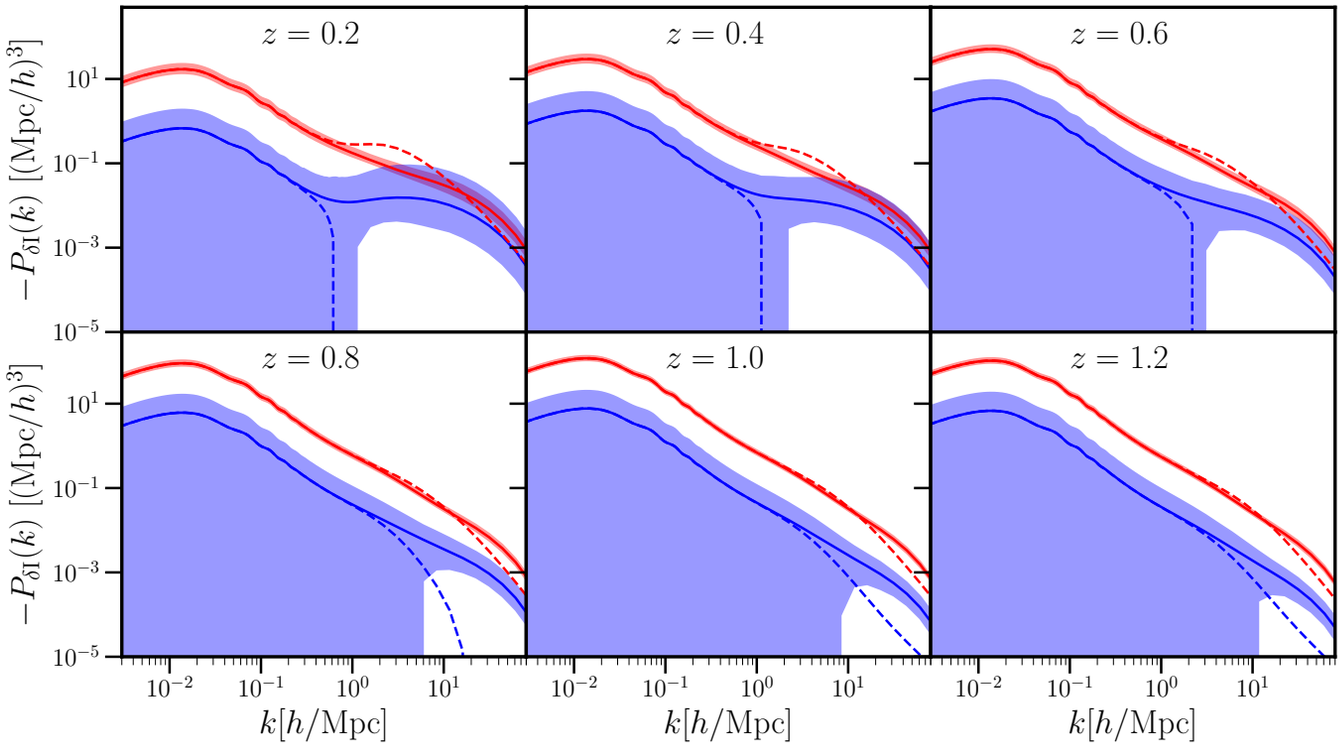

Figure 9. The matter - intrinsic shear power spectrum, for the six redshift bins considered in our analysis. Legend as in Figure 8.

Table 2. Satellite luminosity dependence best fit amplitude (a_{1h}) for the red and blue sample. The samples are split in two luminosity bins, L1 (bright) and L2 (faint), with a cut at $M_r = -22$. In all of the fits, we assume a radial dependence with the form of a power law with slope -2, as in G19. In the joint fit, the luminosity dependence is modelled with a power law with slope ζ, as in eq. 20.

Sample		N_{gal}	a_{1h}	ζ	χ^2/dof
Individual sample fits:					
Red	L1	7505	0.0014 ± 0.0002	-	0.59
	L2	6618	0.0008 ± 0.0002	-	1.76
Blue	L1	5989	0.0008 ± 0.0004	-	1.97
	L2	8778	-0.0002 ± 0.0003	-	0.67
Joint fit:					
Red	all		0.0009 ± 0.0001	0.7 ± 0.2	1.02
Blue	all		0.0006 ± 0.0002	0.5 ± 0.4	1.50

Table 3. The IA parameters adopted in our model.

Sample	Parameter	Value
Red	A_{IA}	5.33 ± 0.60
	β	1.2 ± 0.27
	a_{1h}	0.0012 ± 0.0001
	ζ	0.7 ± 0.2
	b	-2
Blue	A_{IA}	0.21 ± 0.37
	β	0
	a_{1h}	0.0008 ± 0.0003
	ζ	0.5 ± 0.4
	b	-2

observe an inverted trend in the redshift dependence: at high redshifts, where only bright galaxies are observed, the large-scale signal increases due to the luminosity dependence of the red central galaxy alignment. The radial alignment of satellite galaxies shifts the contribution of the 1-halo term to larger k, reducing the impact of the IA at intermediate scales. In Fig. 8-9 we plot the case of constant 1-halo alignment for comparison: here we use the average alignment amplitude measured in KiDS+GAMA groups, $a_{1h}^{red} = 0.007$ and $a_{1h}^{blue} = -0.001$. We note that here we do not apply any correction to the amplitude but simply plot the measured 2D $\langle\epsilon_+\rangle$.

At small scales, the uncertainty in the luminosity dependence of the blue satellite alignment dominates our predictions. We note that the joint constrains on the luminosity and radial dependence of the faint blue sample do not fully capture the measurements, as the curve always remains slightly above the data points (Fig. 7). Indeed, the individual fit for the blue L2 sample is consistent with zero (Table 2). This is driven by the fixed slope of the radial dependence when performing the combined radial and luminosity dependence fit. We find that a steeper radial dependence can capture the measurements better, but given the limited S/N we decided to not adopt separate dependencies for the red and blue samples.

6.1 Impact on lensing

To assess the contamination to the lensing measurements, we use the projected angular power spectra, $C(\ell)$, where ℓ is the 2D angular frequency. In the flat sky approximation, these can be written as:

$$C_{obs}^{(ij)}(\ell) = C_{GG}^{(ij)}(\ell) + C_{GI}^{(ij)}(\ell) + C_{IG}^{(ij)}(\ell) + C_{II}^{(ij)}(\ell) \quad (21)$$

where

$$C_{GG}^{(ij)}(\ell) = \int_0^{\chi_{hor}} d\chi \frac{q^{(i)}(\chi)q^{(j)}(\chi)}{\chi^2} P_{\delta\delta}\left(\frac{\ell}{\chi}, \chi\right), \quad (22)$$

$$C_{GI}^{(ij)}(\ell) = \int_0^{\chi_{hor}} d\chi \frac{q^{(i)}(\chi)p^{(j)}(\chi) + p^{(i)}(\chi)q^{(j)}(\chi)}{\chi^2} P_{\delta I}\left(\frac{\ell}{\chi}, \chi\right), \quad (23)$$

and

$$C_{II}^{(ij)}(\ell) = \int_0^{\chi_{hor}} d\chi \frac{p^{(i)}(\chi)p^{(j)}(\chi)}{\chi^2} P_{II}\left(\frac{\ell}{\chi}, \chi\right). \quad (24)$$

Here, χ denotes the comoving distance, χ_{hor} the comoving distance to the horizon, $p^i(\chi)d\chi$ the distribution of source galaxies in the sample i, normalised to $\int d\chi\ p^i(\chi) = 1$, and $q(\chi)$ is the lensing efficiency, defined as

$$q^i(\chi) = \frac{3H_0^2\Omega_m}{2c^2} \int_\chi^{\chi_h} d\chi'\ p^i(\chi') \frac{\chi' - \chi}{\chi'}\ . \quad (25)$$

To simulate the effect of photometric scatter we generate six Gaussian redshift distributions with a scatter $\sigma_z = 0.05(1+z)$, as described in Chisari et al. (2019). We assume a total shape dispersion of $\sigma_\epsilon = 0.35$.

We compute a fully analytical covariance matrix, as described in Hildebrandt et al. (2018). To be consistent with current cosmic shear analyses, we do not include the IA contribution in the covariance matrix. To generate our predictions, we make use of the latest version of the public available software CosmoSIS[9] (Zuntz et al. 2015). Our results are shown in Fig. 10, where the uncertainties in the model predictions are computed as in sec. 6. Here, for computational reasons, we did not set the lower bound of the II blue central galaxy alignment to zero, but simply used the outcome of the Monte Carlo procedure.

[9] https://bitbucket.org/joezuntz/cosmosis

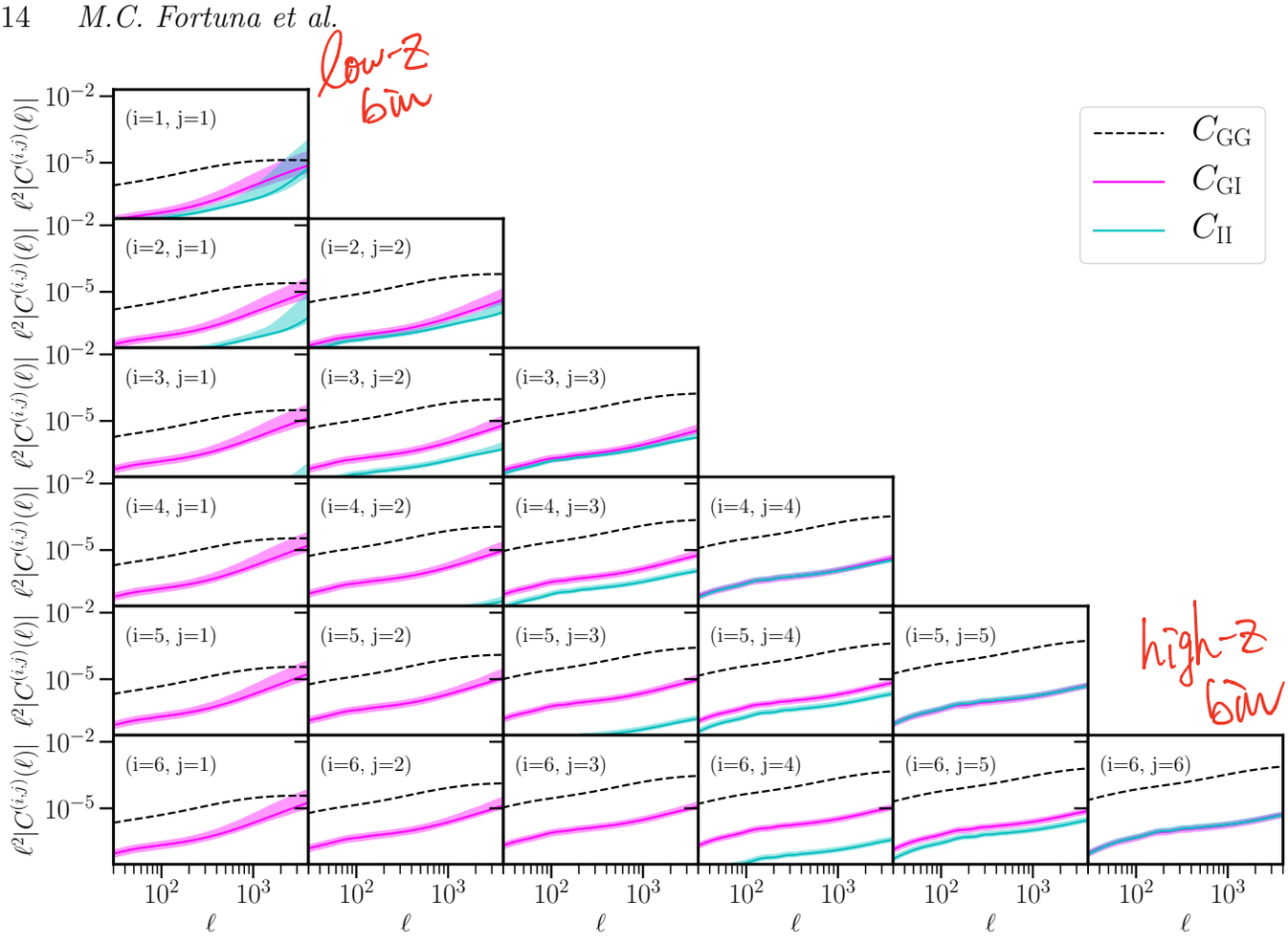

Figure 10. Predictions for the projected angular power spectra. The shaded areas indicate the 1-σ uncertainty on the current constrains on the input parameters. The black dashed line shows the lensing power spectrum.

At low redshift, the large fraction of satellite galaxies is reflected in the IA signal, which becomes important. As expected, the II term is only relevant in the autocorrelation bins, while the GI is larger in all of the off-diagonal terms. Overall, the relative contamination from IA is larger at low redshifts, where also lensing is less efficient.

6.2 The impact of the modelling choice on the cosmological parameter estimate

The main goal of this paper is to investigate whether the emerged complexity of satellite contribution in the IA signal can lead to a bias in the Stage III cosmological parameter estimate if not properly accounted. To explore this, we consider two cases of a generic cosmic shear analysis: in the first we simply assume the NLA model to hold for the full sample, without splitting in red and blue galaxies and without considering any luminosity dependence - so with only one free parameter, the amplitude $A_{\rm IA}$; in the second case we introduce a power law to capture the redshift evolution of the signal due to the IA dependence on the galaxy sample:

$$P_{\delta \rm I}(k,z) = \left(\frac{1+z}{1+z_0}\right)^{\eta} P_{\delta \rm I}^{\rm NLA}(k,z) \tag{26}$$

and

$$P_{\rm II}(k,z) = \left(\frac{1+z}{1+z_0}\right)^{2\eta} P_{\rm II}^{\rm NLA}(k,z), \tag{27}$$

where we choose $z_0 = 0.3$. We refer to this model as NLA-z.

To do so, we generate a data vector of angular correlation functions $\xi_{\pm}(\theta)$ with the setup discussed in Sec. 5 and analyse it assuming the NLA and NLA-z as typically done in most of the Stage III analyses. In this way, we have perfect knowledge of the signal injected and we can isolate the impact of marginalisation.

We perform the analysis in real space, using the projected correlation functions $\xi_{\pm}$, which we derive from the angular power spectra $C(l)$ using the implementation available in CosmoSIS (Kilbinger et al. 2009). The minimum and maximum angular scales adopted in this analysis are, respectively: $\theta_+^{\rm min} = 3'$, $\theta_+^{\rm max} = 72'$, $\theta_-^{\rm min} = 6'$ and $\theta_+^{\rm max} = 153'$, based on the KV450 (Hildebrandt et al. 2018) cosmic shear analysis.

We limit our interest to the cosmological parameters to which lensing is most sensitive, Ω_m and σ_8. Instead of σ_8, we sample the logarithm of the scalar amplitude $\ln(10^{10}A_s)$, so our final parameter vector is $\lambda = \{\Omega_m, \ln(10^{10}A_s)\}$ and one (two) nuisance parameter(s), $A_{\rm IA}$ ($A_{\rm IA}$, η). We adopt uniform priors $\Omega_m = [0.1, 0.8]$, $\ln(10^{10}A_s) = [1.5, 5]$, $A_{\rm IA} =$

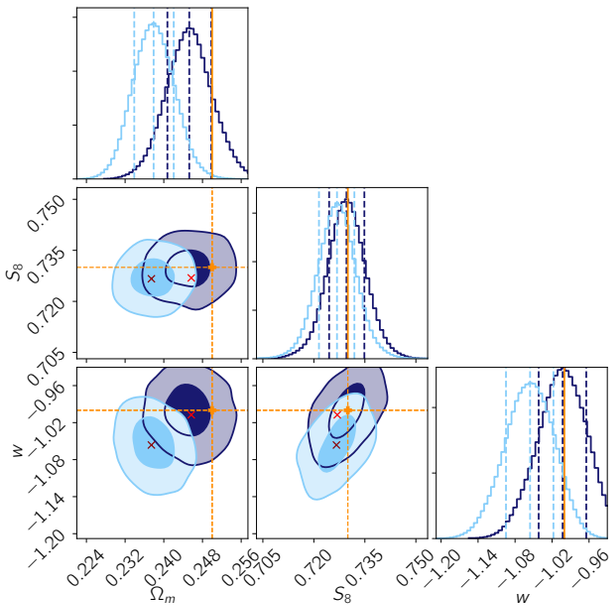

Figure 11. Constraints on the cosmological parameters Ω_m and $S_8 = \sigma_8\sqrt{\Omega_m/0.3}$, marginalising over the IA amplitude, for a Stage IV survey. We inject the IA signal as predicted by the full halo model formalism (see Tab. 3) and perform the analysis assuming a (1) NLA model (dark blue) and (2) no IA signal, $A_{\rm IA} = 0$ (light blue). No distinction between red and blue galaxies is assumed in the analysis. The orange lines and the square marker indicate the fiducial values of the cosmological parameters. The red (NLA) and dark red (no IA) crosses indicate the best fit parameters.

$[-6, 6]$ ($\eta = [-5, 5]$). To sample the parameter space we make use of the EMCEE sampler (Foreman-Mackey et al. 2013).

Our results show that for the case of Stage III surveys, the NLA model provides a sufficient description, and the redshift dependence of the IA caused by the variation of the galaxy sample is not large enough to induce a bias in the cosmological parameters. We find a remarkably small value for the best fit IA amplitude, which is compatible with zero (NLA: $A_{\rm IA} = 0.1^{+0.1}_{-0.1}$). With a best fit amplitude $A_{\rm IA} \sim 0$, the η parameter of the NLA-z model remains completely unconstrained so that the two models are equivalent.

Our findings are in line with the best fit NLA amplitude found in J19 for the full GAMA sample, while their best fit value for the joint GAMA+SDSS Main has an amplitude of $A_{\rm IA} \sim 1$, compatible with the fact that SDSS Main has fewer satellite galaxies to lower the signal at large scales. Our lower amplitude is consistent with the fact that our sample is fainter than GAMA and contains more satellites. The comparison is however complicated by the fact that J19's measurements are performed on the gI correlation. Compared to the KV450 IA amplitude, $A_{\rm IA} = 0.981^{+0.694}_{-0.678}$, we find a lower value for a similar galaxy sample. However, different redshift distributions are adopted in the two works. We note that the full shape of the $n(z)$ is critical for the accurate modelling of the IA contribution (see Appendix C). The redshift distributions of KV450 are more peaked and with more prominent tails, which increase the impact of the II in real data: as a consequence, since II and GI have opposite contributions, the IA balance changes. Moreover, a luminosity dependence of the signal reduces the presence of IA in the data (Joachimi et al. 2011; Krause et al. 2016): if the faint end of the luminosity dependence of red central galaxies is significantly shallower than what assumed in this work, the final amplitude would increase. Similarly, our predictions are based on the assumption that the blue central galaxy population does not significantly contribute to the signal ($A_{\rm IA}^{\rm blue} = 0.21$), a constraint that suffers from large uncertainties.

Given our results on a Stage III setup, we investigate whether in the case of a Stage IV survey we still recover the right cosmological parameters. We leave our setup unchanged, and only replace the covariance matrix to account for the larger area (15 000 deg^2) and double the number density per redshift bin. In this case, we also allow w to vary, assuming a uniform prior $w \in [-5.0, 0.33]$. Our results are illustrated in Fig. 11 (dark blue contours). We find a 1σ bias on Ω_m, while the other parameters are correctly recovered. The comparison with the case of no IA (light blue contours), shows that even if the overall IA signal is small, not accounting for it introduces more than 1σ bias in both Ω_m and w.

7 CONCLUSIONS

We have performed a comprehensive analysis of the contamination by IA in cosmic shear surveys, with a particular focus on modelling the satellite contributions at small and large scales, based on the most recent observational IA findings. We proposed a new model to describe the IA signal, which explicitly accounts for the fact that only red central galaxies contribute to the alignment signal at large scales. We introduced a satellite alignment signal at small scales, modelled through the halo model formalism, and which includes a radial and luminosity dependence.

At large scales, we investigated whether limiting a luminosity dependence of the IA signal to the central galaxy sample provides a unified picture for all the measurements in the literature. Although in this scenario the slope measured by MegaZ/LOWZ seems to be favoured, we want to stress that the current uncertainty in the measurements does not allow for a definitive constraint on the luminosity dependence. Future IA studies should focus on constraining the faint end of Fig. 5, where uncertainties dominate. Upcoming surveys such as the Physics of the Accelerating Universe Survey[10] (PAUS; Eriksen et al. 2019; Padilla et al. 2019) can help gaining insight into our understanding of the faint central galaxy alignment, a key feature to properly predict the IA contamination in cosmic shear surveys.

At small scales, we model the satellite alignment with a power law for the radial dependence, as recently measured by G19 in groups. We re-analyse the G19 data splitting the sample in red and blue, and we found that in this case a cut at $M_r = -22$ suggests a luminosity dependence in the signal. We jointly fitted the radial and luminosity dependence assuming a double power law, and used this result as input for our forecasting model. More data are needed

[10] https://www.pausurvey.org

to tightly constrain the luminosity dependence of satellites, as the statistical uncertainties in the measurements might play a role in constraining the amplitude of the power law. It is also relevant to note that since red and blue satellites show a different alignment amplitude, it is crucial to model them separately, as their relative fraction depends on the magnitude cut of the specific survey.

Although satellites do not share the same alignment mechanisms as central galaxies, the morphology dichotomy observed at large scales is reflected also in their alignment mechanism. A different radial dependence of red and blue satellites might reveal a more complex alignment mechanism for the two populations and/or probe the galaxy in-fall history. With current measurements it is not possible to further investigate this possibility, but future dedicated high resolution hydrodynamical simulations might shed light in the understanding of the intra-halo alignment.

Our predicted power spectra show two opposite trends at high and low redshifts, as shown in Fig. 8 and 9. While at low redshift the small scales have a larger IA signal, due to the presence of satellites, the large scales are dominated by the alignment of red central galaxies. The large scale signal becomes stronger as we go to higher redshifts, due to the survey magnitude cut: this selects brighter galaxies, which are those that carry most of the IA signal, due to the observed luminosity dependence of the red central galaxy alignment. The opposite happens to the small scales, which are almost completely washed out by the suppression of satellites in the high redshift bins.

In this work we have not accounted for the anisotropic distribution of satellites within the halo, which is also known to contaminate lensing measurements. In the context of cosmic shear analyses, this is expected to be important only at small and intermediate scales. The satellite segregation along the central galaxy major axis complicates the interpretation of IA measurements performed using the central galaxy position - satellite shear correlation (gI), and future studies should focus on modelling it, in order to have a clear mapping between gI and GI. However, our spherical model can be considered as an *effective* model: in the perspective of a direct fit of IA to data, the free amplitude in the 1-halo term can potentially capture to first order the extra correlation due to the anisotropic term.

While direct IA measurements provide unique insights into the IA mechanisms and amplitudes, translating those results into informative priors for cosmic shear analyses requires a full modelling of the sample dependence of the IA signal. This aspect has often been underestimated in lensing studies, adopting simplistic models that do not distinguish between the different IA signatures of different galaxy populations, and adopting broad, uninformative priors. We investigated what is the impact of this choice for the IA signal that we expect for a cosmic shear survey given our model. We considered the case of a Stage III analysis on a simulated data vector, built to reproduce our best knowledge of the IA, and then analysed it using simple NLA and NLA$-z$ models. Limiting our analysis to Ω_m, S_8, we find the NLA model to be sufficient to capture the IA signal without biasing in the cosmological parameters. This is no longer true for Stage IV surveys, where we observe a 1σ bias in Ω_m. We find the IA amplitude recovered by those models to be in all cases compatible with zero. Overall, we find the IA signal to be smaller than what assumed in previous works. This propagates in the level of bias that we observe for the cosmological parameters. We want to stress that these findings are based on several assumptions which represent our best extrapolation of the current picture of IA as emerging from dedicated studies. Future studies on the behaviour of faint central and satellite galaxies are needed to confirm these results. However, the model is extremely flexible and any new findings can be easily incorporated.

We made our forecasts using IA priors that come from the best fit values constrained by observations, without accounting for their current uncertainties. We leave the investigation of which parameter of the IA model is driving the bias in the Ω_m in a *Euclid* tailored setup to a forthcoming paper.

We want to stress that these model predictions are based on idealised redshift distributions and so our results cannot be directly compared with the best fit parameters inferred by cosmic shear studies. At higher redshifts and lower luminosities, the mocks might suffer from a larger uncertainty, as the luminosity is calibrated locally and then evolved to high redshifts. This has to be considered as part of the uncertainty in the model predictions, which requires additional data to be assessed. Upcoming surveys that aim to use the model can use clustering information in their data and the observed luminosity function to further constrain these parameters.

In light of future cosmological analyses, this model can be used to account for the IA signatures on different galaxy populations allowing for the use of informative priors from specific sample selected analyses. Given a halo occupation distribution model for the red and blue galaxy populations, this model can be employed to jointly fit the clustering, IA and lensing observables.

ACKNOWLEDGEMENTS

We thank Shahab Joudaki and Francisco Castander for useful discussions and comments and Kai Hoffmann for providing comments on a preliminary version of this manuscript. MCF and HH acknowledge support from Vici grant 639.043.512, financed by the Netherlands Organisation for Scientific Research (NWO). HH also acknowledges funding from the EU Horizon 2020 research and innovation programme under grant agreement 776247.

The MICE simulations have been developed at the MareNostrum supercomputer (BSC-CNS) thanks to grants AECT-2006-2-0011 through AECT-2015-1-0013. Data products have been stored at the Port d'Informació Científica (PIC), and distributed through the CosmoHub webportal (cosmohub.pic.es). Funding for this project was partially provided by the Spanish Ministerio de Ciencia e Innovacion (MICINN), projects 200850I176, AYA2009-13936, AYA2012-39620, AYA2013-44327, ESP2013-48274, ESP2014-58384 , Consolider-Ingenio CSD2007- 00060, research project 2009-SGR-1398 from Generalitat de Catalunya, and the Ramon y Cajal MICINN program.

Based on data products from observations made with ESO Telescopes at the La Silla Paranal Observatory under programme IDs 177.A- 3016, 177.A-3017 and 177.A-3018, and on data products produced by Tar- get/OmegaCEN,

INAF-OACN, INAF-OAPD and the KiDS production team, on behalf of the KiDS consortium. OmegaCEN and the KiDS production team ac- knowledge support by NOVA and NWO-M grants. Members of INAF-OAPD and INAF-OACN also acknowledge the support from the Department of Physics & Astronomy of the University of Padova, and of the Department of Physics of Univ. Federico II (Naples). GAMA is a joint European-Australasian project based around a spectroscopic campaign using the Anglo-Australian Telescope. The GAMA input catalogue is based on data taken from the Sloan Digital Sky Survey and the UKIRT Infrared Deep Sky Survey. Complementary imaging of the GAMA regions is being obtained by a number of independent survey programmes including GALEX MIS, VST KiDS, VISTA VIKING, WISE, Herschel-ATLAS, GMRT and ASKAP providing UV to radio coverage. GAMA is funded by the STFC (UK), the ARC (Australia), the AAO, and the participating institutions. The GAMA website is `http://www.gama-survey.org/`.

REFERENCES

Abell P. A., et al., 2009
Bartelmann M., Schneider P., 2001, Phys. Rep., 340, 291
Blanton M. R., et al., 2003, ApJ, 592, 819
Blanton M. R., et al., 2005, AJ, 129, 2562
Bridle S., King L., 2007, New Journal of Physics, 9, 444
Carretero J., Castander F. J., Gaztañaga E., Crocce M., Fosalba P., 2015, MNRAS, 447, 646
Catelan P., Kamionkowski M., Blandford R. D., 2001, MNRAS, 320, L7
Chisari N. E., Mandelbaum R., Strauss M. A., Huff E. M., Bahcall N. A., 2014, MNRAS, 445, 726
Chisari N. E., Dunkley J., Miller L., Allison R., 2015a, MNRAS, 453, 682
Chisari N., et al., 2015b, MNRAS, 454, 2736
Chisari N. E., et al., 2019, ApJS, 242, 2
Codis S., Jindal A., Chisari N. E., Vibert D., Dubois Y., Pichon C., Devriendt J., 2018, MNRAS, 481, 4753
Crocce M., Castander F. J., Gaztañaga E., Fosalba P., Carretero J., 2015, MNRAS, 453, 1513
Driver S. P., et al., 2011, MNRAS, 413, 971
Duffy A. R., Schaye J., Kay S. T., Dalla Vecchia C., 2008, MNRAS, 390, L64
Eriksen M., et al., 2019, MNRAS, 484, 4200
Foreman-Mackey D., Hogg D. W., Lang D., Goodman J., 2013, PASP, 125, 306
Fosalba P., Crocce M., Gaztañaga E., Castand er F. J., 2015, MNRAS, 448, 2987
Georgiou C., et al., 2019a, arXiv e-prints, p. arXiv:1905.00370
Georgiou C., et al., 2019b, A&A, 622, A90
Hildebrandt H., et al., 2018, arXiv e-prints, p. arXiv:1812.06076
Hirata C. M., Seljak U., 2004, Phys. Rev. D, 70, 063526
Hirata C. M., Mandelbaum R., Ishak M., Seljak U., Nichol R., Pimbblet K. A., Ross N. P., Wake D., 2007, MNRAS, 381, 1197
Huang H.-J., Mandelbaum R., Freeman P. E., Chen Y.-C., Rozo E., Rykoff E., Baxter E. J., 2016, MNRAS, 463, 222
Huang H.-J., Mandelbaum R., Freeman P. E., Chen Y.-C., Rozo E., Rykoff E., 2018, MNRAS, 474, 4772
Joachimi B., Bridle S. L., 2010, A&A, 523, A1
Joachimi B., Mandelbaum R., Abdalla F. B., Bridle S. L., 2011, A&A, 527
Joachimi B., et al., 2015, Space Sci. Rev., 193, 1
Johnston H., et al., 2019, A&A, 624, A30
Kannawadi A., et al., 2019, A&A, 624, A92
Kiessling A., et al., 2015, Space Sci. Rev., 193, 67
Kilbinger M., 2015, Reports on Progress in Physics, 78, 086901
Kilbinger M., et al., 2009, A&A, 497, 677
Kirk D., Bridle S., Schneider M., 2010, MNRAS, 408, 1502
Kirk D., et al., 2015, Space Sci. Rev., 193, 139
Kraljic K., Dave R., Pichon C., 2019, arXiv e-prints, p. arXiv:1906.01623
Krause E., Eifler T., Blazek J., 2016, MNRAS, 456, 207
Kravtsov A. V., Berlind A. A., Wechsler R. H., Klypin A. A., Gottlöber S., Allgood B., Primack J. R., 2004, ApJ, 609, 35
Kuijken K., et al., 2019, A&A, 625, A2
Laureijs R., et al., 2011, arXiv e-prints, p. arXiv:1110.3193
Mandelbaum R., 2018, Annual Review of Astronomy and Astrophysics, 56, 393
Mandelbaum R., Hirata C. M., Ishak M., Seljak U., Brinkmann J., 2006, Mon. Not. R. Astron. Soc, 367, 611
Mandelbaum R., et al., 2011, MNRAS, 410, 844
Melchior P., Viola M., Schäfer B. M., Bartelmann M., 2011, MNRAS, 412, 1552
Murray S., 2014, HMF: Halo Mass Function calculator (ascl:1412.006)
Navarro J. F., Frenk C. S., White S. D. M., 1996, ApJ, 462, 563
Padilla C., et al., 2019, AJ, 157, 246
Pereira M. J., Bryan G. L., 2010, ApJ, 721, 939
Pereira M. J., Bryan G. L., Gill S. P. D., 2008, ApJ, 672, 825
Piras D., Joachimi B., Schäfer B. M., Bonamigo M., Hilbert S., van Uitert E., 2018, MNRAS, 474, 1165
Samuroff S., et al., 2018, arXiv e-prints, p. arXiv:1811.06989
Samuroff S., Mandelbaum R., Di Matteo T., 2019, arXiv e-prints, p. arXiv:1901.09925
Schneider M. D., Bridle S., 2010, MNRAS, 402, 2127
Sifón C., Hoekstra H., Cacciato M., Viola M., Köhlinger F., van der Burg R. F. J., Sand D. J., Graham M. L., 2015, A&A, 575, A48
Sifón C., Herbonnet R., Hoekstra H., van der Burg R. F. J., Viola M., 2018, MNRAS, 478, 1244
Singh S., Mandelbaum R., More S., 2015, MNRAS, 450, 2195
Skibba R. A., Sheth R. K., 2009, MNRAS, 392, 1080
Soussana A., et al., 2020, MNRAS, p. 58
Tenneti A., Mandelbaum R., Di Matteo T., 2016, MNRAS, 462, 2668
Tenneti A., Gnedin N. Y., Feng Y., 2017, ApJ, 834, 169
Tinker J. L., Robertson B. E., Kravtsov A. V., Klypin A., Warren M. S., Yepes G., Gottloeber S., 2010, The Astrophysical Journal, 724, 878
Tonegawa M., Okumura T., Totani T., Dalton G., Glazebrook K., Yabe K., 2018, PASJ, 70, 41
Troxel M. A., Ishak M., 2015, Phys. Rep., 558, 1
Zehavi I., et al., 2011, ApJ, 736, 59
Zheng Z., et al., 2005, The Astrophysical Journal, 633
Zuntz J., et al., 2015, Astronomy and Computing, 12, 45
de Jong J. T. A., Verdoes Kleijn G. A., Kuijken K. H., Valentijn E. A., 2013, Experimental Astronomy, 35, 25
van Uitert E., Joachimi B., 2017, MNRAS, 468, 4502
van Uitert E., Cacciato M., Hoekstra H., Herbonnet R., 2015, A&A, 579, A26

APPENDIX A: SATELLITE GALAXY FRACTIONS IN MICE

We investigate here how well MICE reproduces the GAMA survey in the corresponding redshift and magnitude space, because we use that sample as input for our study. Our reference GAMA catalogue is obtained by matching the StellarMassLambda-v2 catalogue, from which we obtain

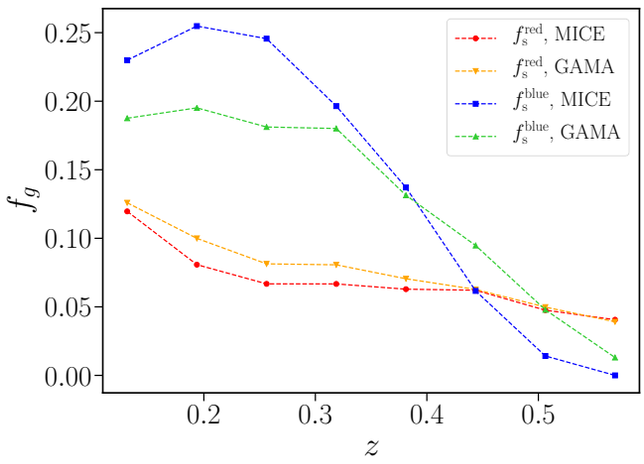

Figure A1. The satellite galaxy fractions in our mocks compared to those in the GAMA sample. We select the galaxies in the mocks to reproduce the same redshift-magnitude selection as GAMA.

photometric information, and the G3CGal, which contains the group information. We identify the satellite population by imposing RankBCG>1.

We build a GAMA-like sample from MICE in the following way. We select from our mock all galaxies brighter that $r < 19.8$, the flux-limit of our GAMA catalogue, and limited the analysis to a sub-patch of ~ 180 deg^2, which is the size of the overlapping region with the KiDS survey employed by J19, C19 and in this work. With only these conditions, we find a very good agreement with the colour and magnitude distributions of the GAMA galaxies.

Given the compatibility in the colour-magnitude space, we select red galaxies in GAMA by applying the same cut as used in the rest of the paper (2.1). We then measure the galaxy fraction for all the sub-samples that enter in the halo model, to quantify the accuracy of our mocks. Fig. A1 illustrates our findings. We observe a remarkable agreement for the red galaxy population. For the blue sample, MICE exhibits a larger satellite fraction at low redshift and the opposite behaviour at high redshifts; however, the absolute difference between the fractions found in MICE and GAMA is 0.065 at maximum.

APPENDIX B: THE ANGULAR PART OF THE SATELLITE ALIGNMENT DENSITY RUN

We compute the satellite alignment following the formalism developed in Schneider & Bridle (2010), assuming a perfect radial alignment scenario. We report here our expansion for f_l and the main steps to derive it. Fig B1 shows the comparison between our result and the analytical solution for the first multipoles ($l_{\rm max} = 4$).

The complex phase in equation 13 can be re-written through the plane wave expansion:

$$\exp(i\mathbf{k}\cdot\mathbf{r}) = \sum_{l=0}^{\infty} i^l (2l+1) P_l(\cos\gamma) j_l(kr)\,, \tag{B1}$$

where $P_l(x)$ are the Legendre polynomials of order l and $\cos\gamma$ is the angle between $\mathbf{r} = (r, \theta, \phi)$ and $\mathbf{k} = (k, \theta_k, \phi_k)$,

$$\cos\gamma = \sin\theta_k \sin\theta \cos(\phi_k - \phi) + \cos\theta_k \cos\theta\ . \tag{B2}$$

We can rewrite the Legendre polynomials through the identity

$$P_l(x) = 2^l \sum_{m=0}^{l} x^m \binom{l}{m} \binom{\frac{l+m-1}{2}}{l}\,, \tag{B3}$$

where $x = \cos\gamma$. We can express $(\cos\gamma)^m$ using the binomial theorem, such that all of the terms on the right in equation B2 are of the form a^j and those on the left b^{m-j}, where j goes from 0 to m. Separating the integrals on ϕ and θ, we have that the azimuthal part reduces to

$$\int_0^{2\pi} \mathrm{d}\phi \binom{\cos(2\phi)}{\sin(2\phi)} (\cos\phi_k \cos\phi + \sin\phi_k \sin\phi)^j\ , \tag{B4}$$

where the integrals over ϕ are all zeros for odd j, while the even terms are

$$g_{j=2n} = \left\{0, \frac{\pi}{2}, \frac{\pi}{2}, \frac{15\pi}{32}, ...\right\} \text{ for n=1,2,3, } \ldots\ . \tag{B5}$$

The terms in ϕ_k can be rearranged to be of the form $\mathrm{e}^{i2\phi_k}$. The integral over the polar angle θ gives instead

$$\begin{aligned}\int_{-1}^{1} \mathrm{d}\cos\theta \sin^{j+1}\theta \cos^{m-j}\theta &= \int_{-1}^{1} \mathrm{d}\cos\theta \left(1-\cos^2\theta\right)^{\frac{j+1}{2}} \cos^{m-j}\theta \\ &= I(j+1, m-j)\,,\end{aligned} \tag{B6}$$

where, following SB10, we have defined

$$I(a,b) = \int_{-1}^{1} \mathrm{d}x (1-x^2)^{\frac{a}{2}} b^j. \tag{B7}$$

Collecting all the terms together, we get

$$\begin{aligned}f_l(\theta_k, \phi_k) = \mathrm{e}^{i2\phi_k} 2^l \sum_{m=0}^{l} \binom{l}{m} \binom{\frac{l+m-1}{2}}{l} \sum_{j=0}^{m} \binom{m}{j} g_j \\ \times I(j+1, m-j) \sin^j\theta_k \cos^{m-j}\theta_k\ .\end{aligned} \tag{B8}$$

Since the $E-$ and $B-$ modes of the intrinsic alignment are invariant under rotation in the plane of the sky, we can choose without loss of generality to fix $\phi_k = 0$. The polar angle θ_k defines the projection of the wave vector $\mathbf{k}$ on the plane of the sky: modes perpendicular to the line of sight are identified by $\theta_k = \frac{\pi}{2}$, for which we have the strongest alignment signal, as illustrated in Fig. B2. Indeed, the angular part of $w(\mathbf{k}, M)$ (see eq. B5 in SB10) is dominated by the lowest term of the expansion, $l = 2$, which peaks at $\theta_k = \pi/2$, as it is visible in Fig. B1. The main effect of θ_k is to change the amplitude of $w(\mathbf{k}, M)$ (Fig. B2). We decide to assume $\theta_k = \frac{\pi}{2}$ throughout our analysis, i.e. to only consider the modes perpendicular to the line of sight, and to truncate the expansion at $l_{\rm max} = 6$.

Note that we decide to not adopt the definition of the density-weighted shear in SB10, $w(k|M)$ and instead work with their original definition (their equation 7), from which we can naturally derive the expression for the radially dependent case. Here, we normalise the density-weighted shear with the NFW mass, as originally in eq. 7 of SB10.

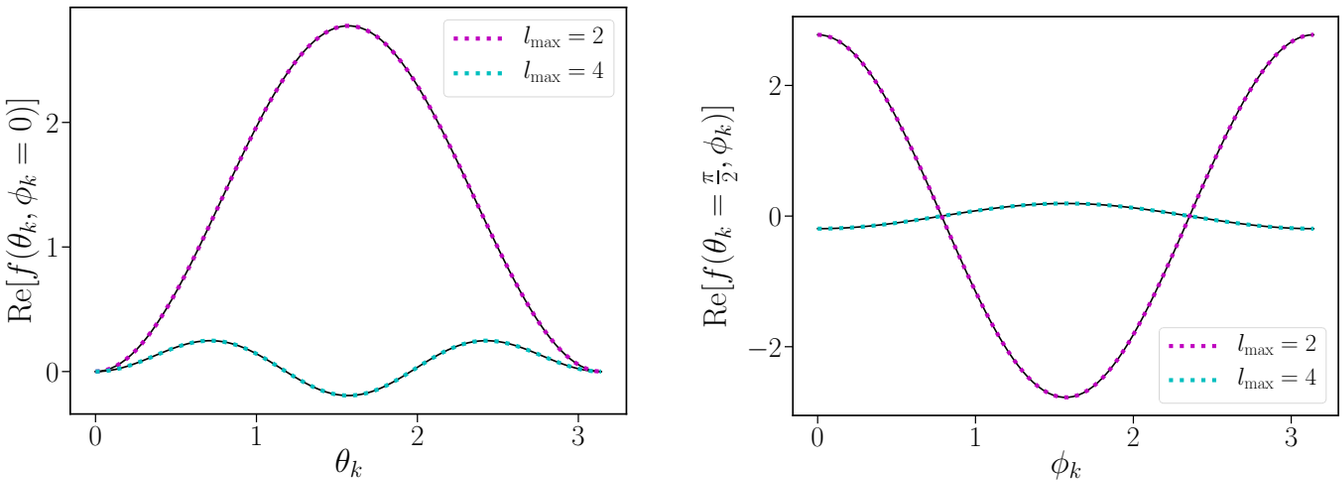

(a) (b)

Figure B1. The angular part of the satellite ellipticity run $w(\mathbf{k}, M)$, $f_l(\theta_k, \phi_k)$. The dotted lines show the first two multipoles of the expansion of f_l as computed in eq. B8. The solid black lines show the same terms as directly derived from the integration of the analytic expression of the P_l ($l = 2, 4$). (a): The dependence of f_l on θ_k at fixed ϕ_k ($\phi_k = 0$). (b): same as (a) but fixing $\theta_k = \frac{\pi}{2}$. Both panels shows only the real part of f_l. We have also checked that the imaginary parts are in agreement with the analytical solution.

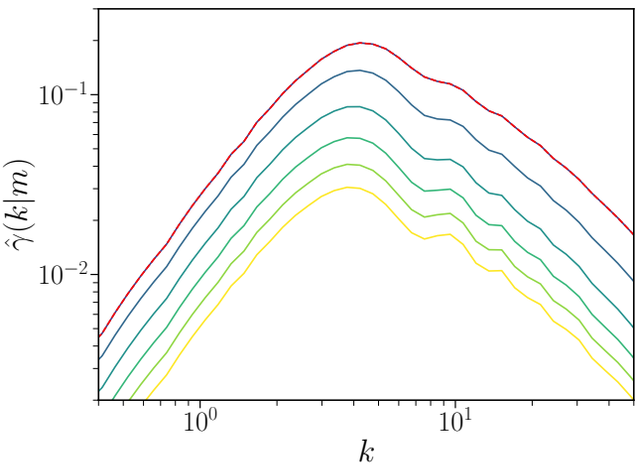

Figure B2. The Fourier transform of the density-weighted shear (eq. 13) for $\phi_k = 0$ and $\theta_k \in \left[\frac{\pi}{2}, \pi\right]$, in the case of constant radial dependence. For clarity, we normalise the curves by the input amplitude, $a_{\rm 1h}$. The amplitude of the curves decreases as we go from $\theta_k = \frac{\pi}{2}$ (red) to $\theta_k = \pi$. Note that $f(\theta_k)$ is symmetric around $\theta_k = \pi/2$, so the curves from $\left[0, \frac{\pi}{2}\right]$ coincide with the ones plotted here, with increasing amplitude for increasing values of θ_k.

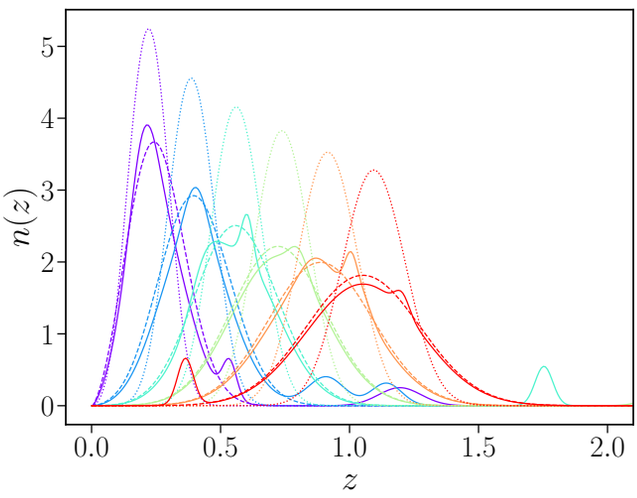

Figure C1. Two of the four different $n(z)$ adopted in our comparison. The dotted curves refer to the case of Gaussian photometric distributions with $\sigma_z = 0.05(1+z)$ as discussed in the text (see sec. 6.1), the dashed curves to broader Gaussians ($\sigma_z = 0.1(1+z)$), while the solid lines are the $n(z)$ built from the broader Gaussians with the inclusion of 'catastrofic outliers' and more pronunced peaks in the distributions.

APPENDIX C: INTRINSIC ALIGNMENT DEPENDENCE ON PHOTOMETRIC REDSHIFT DISTRIBUTIONS

We illustrate here the impact on the choice of $n(z)$ in predicting the IA signal. As discussed in Sec. 6, the specific choice of the $n(z)$ distribution plays an important role in enhancing the II term, changing the balance between the different IA components. Here, we try to disentangle which feature has the largest impact on modulating the magnitude of the II term and its scale dependence. We generate three different distributions (C1), which progressively include a new feature. Fig. C2 illustrates our findings. We start with the Gaussian distributions adopted in the paper and presented in Sec. 6.1 (solid orange lines), then we broaden them by increasing the standard deviation per bin, $\sigma_z^{\rm broad} = 0.1(1+z)$ (dashed green lines): this increases the amplitude of the II power spectra in the off-diagonal terms, due to the overlap of the tails of the distributions from different adjacent bins; on the diagonal terms, the broadening slighly reduces the II power spectrum. We then introduce 'catastrophic outliers', which we generate as Gaussian islands centred on random points extracted from the original dN/dz, with a similar ap-

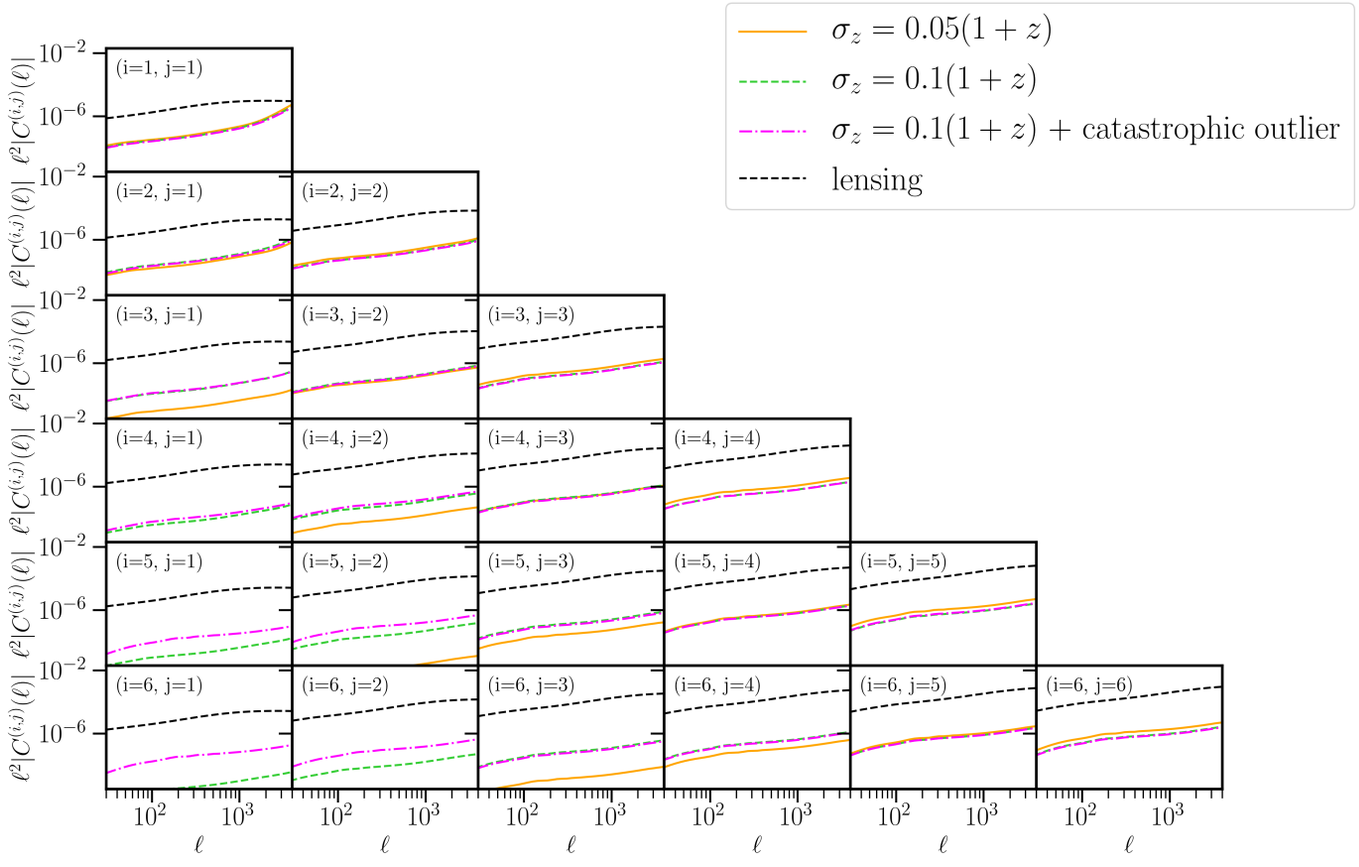

Figure C2. The impact of the $n(z)$ on the projected II angular power spectrum. The IA is generated assuming the same setup as 3, while the $n(z)$ are respectively: the fiducial Gaussian $n(z)$ adopted in the rest of the paper (solid orange lines), broader Gaussian distributions (dashed green lines) and borader Gaussians with the superpositions of 'catastrophic outliers' and peaks (dash-dotted magenta lines). The lensing signal (black, dotted lines) is reported for reference and it is computed assuming the fiducial $n(z)$.

proach as Samuroff et al. (2019). The presence of the outliers increases the II contribution (dash-dotted magenta lines): this is particular prominent at low redshift, for highly separated $z-$bins, where the outliers introduce correlated pairs between bins that would otherwise been uncorrelated.

This paper has been typeset from a TEX/LATEX file prepared by the author.